TEMPERATURE-DEPENDENT PROPERTIES OF FLUORESCENCE SPECTRA OF GROUP-IV DIAMOND COLOR CENTERS

A Dissertation

by

CHRISTAPHER NICHOLAS VINCENT

Submitted to the Graduate and Professional School of
Texas A&M University
in partial fulfillment of the requirements for the degree of

DOCTOR OF PHILOSOPHY

Chair of Committee,	Alexey Zheltikov
Committee Members,	Alexei Sokolov
	Philip Hemmer
	Olga Kocharovskaya
Head of Department,	Grigory Rogachev

May 2023

Major Subject: Physics

ABSTRACT

The amount of thermal energy that a system possesses, otherwise known as its temperature, is a property whose measurement has been utilized in experiments since Galileo constructed his first thermoscope. Over the centuries succeeding Galileo, scientific advancements lea to improved measurement methodologies and apparatuses. This allowed measurements with increased accuracy and sensitivity, coupled with decreased sensor size and acquisition time. A recent advancement in this field is optical thermometry, which utilizes fluorescing color centers in diamonds. The stalwart of optical thermometry is the utilization of optical detection of magnetic resonance (ODMR) of nitrogen–vacancy (NV) color centers. This method's main drawback is its use of microwave fields to measure the electron spin resonance (ESR) of the color center, which is detrimental to *in vivo* measurements. An alternative method is to use heavier Group-IV elements to create a split vacancy color center. These color centers have spectra whose zero phonon lines (ZPL's) and phonon sidebands (PSB's) have a high enough contrast ratios to perform all-optical fluorescence thermometry. By quantifying the temperature dependence of various properties (peak width, central wavelength, amplitude, and Debye–Waller factor (DWF)) of their photoluminescence (PL) spectral peaks, these color centers have been used as thermometers with high spatial resolution, precision, and sensitivity without the drawbacks of NV based thermometers. One such color center, germanium–vacancy (GeV), has been found to have a precision of 0.008 nm/K, sensitivities in the range of a few $\mathrm{mK}/\sqrt{\mathrm{Hz}}$, and a spatial resolution on the micron scale; although, better sensitivities and higher spatial resolutions are possible. While these color centers avoid the damages incurred by the ODMR measurements, they are still hindered by a heating penalty induced by linear laser radiation absorption from the pump laser. The relationship between pump power and fluorescence brightness, coupled with the relationship between fluorescence brightness and sensitivity, leads to the incurring of a substantial heating penalty for increased sensitivity in measurements. Another split-vacancy color center, nickel–vacancy (NiV), operates in the near-infrared (near-IR), which can penetrate farther through biological materials than the optical PL of Group-IV color centers.

DEDICATION

To my mother and father for instilling the thirst, desire, and respect for knowledge and education. To my grandmother (RIP), for always excitedly listening to me explain my work, even while understanding none of it. To my cat, Agrajag, for keeping me company and humble (she could not care less about my degrees).

ACKNOWLEDGMENTS

I would like to thank Dr. Marlon Scully for inspiring me to attend Texas A&M University and Dr. Sayandeb Basu for helping me get here.

CONTRIBUTORS AND FUNDING SOURCES

Contributors

This work was supported by a thesis committee consisting of Professor Aleksei Zheltikov, Professor Alexei Sokolov, and Distinguished professor Olga Kocharovskaya, of the Department of Physics and Astronomy and Professor Philip Hemmer of the Department of Electrical and Computer Engineering.

Experiments were performed in concert with Dr. Sean Blakley, Dr. Ilya Fedotov, Xinghua Liu, Ajithamithra Dharmasiri, Tanvir Rajib, Dr. Dawson Nodurft, Dr. Xiaohan Liu, Dr. Ivan Cojocaru, and Jiru Liu.

All other work conducted for the thesis (or) dissertation was completed by the student independently.

Funding Sources

Graduate study was supported by a grant from the Welch Foundation (A-1801-20180324).

TABLE OF CONTENTS

Page

ABSTRACT ii

DEDICATION iii

ACKNOWLEDGMENTS iv

CONTRIBUTORS AND FUNDING SOURCES v

TABLE OF CONTENTS vi

LIST OF FIGURES viii

1. INTRODUCTION AND LITERATURE REVIEW 1

    1.1 Statement 1
    1.2 State of the art 6

2. BACKGROUND 10

    2.1 Motivation 10
    2.2 Statement of problem 10
    2.3 Tools 11
        2.3.1 Group-IV split-vacancy color centers as eleven electron systems 11
        2.3.2 Temperature dependent behaviors of split-vacancy color center spectral properties 12
            2.3.2.1 Line shift 12
            2.3.2.2 Peak broadening 13
            2.3.2.3 Temperature dependence of peak amplitude 14
            2.3.2.4 Temperature dependence of DWF 16
            2.3.2.5 Wrap up 17

3. RESULTS 18

    3.1 Fiber probe spectroscopy 19
    3.2 Split-spectrum intensity integration 23
    3.3 Open-air spectroscopy 25
    3.4 Nickel–Vacancy open-air spectroscopy 29

4. CODA 32

4.1 applications 32
4.2 Future explorations 33
4.2.1 Improved fittings 33
4.2.2 Optical gating 33
4.3 Conclusion 34

REFERENCES 35

APPENDIX A. LIST OF PUBLICATIONS 38

APPENDIX B. SUPPLEMENT 2: TEMPERATURE DEPENDENCE OF ELECTRON–PHONON PROCESSES IN SPLIT-VACANCY COLOR CENTERS AND THEIR EFFECTS ON SPECTRAL PEAK PROPERTIES 39
B.0.1 Relaxation rates and peak broadening 40
B.0.2 Spin-orbit splitting and central wavelength shifts 41

LIST OF FIGURES

FIGURE Page

1.1 Thermal History 2

1.2 Diamond Growth 5

1.3 State of the Art Thermometry 7

2.1 Group-IV Split-Vacancy Energy Levels 11

2.2 GeV Line Shift Thermal Dependence 13

2.3 GeV Peak Broadening Thermal Dependence 14

2.4 GeV Linear Approximations 14

2.5 GeV Spectral Deconstruction 17

3.1 '*Fiber-Optic Quantum Thermometry with Germanium-Vacancy Centers in Diamond*' (1) 20

3.2 '*Fiber-Optic Quantum Thermometry with Germanium-Vacancy Centers in Diamond*' (2) 20

3.3 '*Photonic-Crystal-Fiber Quantum Probes for High-Resolution Thermal Imaging*'(1) 21

3.4 '*Photonic-Crystal-Fiber Quantum Probes for High-Resolution Thermal Imaging*'(1) 22

3.5 Split-spectrum intensity integration (1) 24

3.6 Split-spectrum intensity integration (2) 25

3.7 Split-spectrum intensity integration (3) 26

3.8 Open-air spectroscopy (1) 27

3.9 Open-air spectroscopy (2) 28

3.10 NiV Spectroscopy (1) 29

3.11 NiV Spectroscopy (2) 30

3.12 NiV Spectroscopy (3) 30

3.13 NiV Spectroscopy (4) 31

4.1 '*Photonic toolbox for fast real-time polymerase chain reaction*' 32

4.2 GeV Optical Gating 33

B.1 Group-IV Split-Vacancy Electron–Phonon Processes 39

1. INTRODUCTION AND LITERATURE REVIEW

1.1 Statement

In 1586, possibly after reading up on Hero's work, Galileo Galilei created what could be considered humanity's first step towards thermal measurements with the creation of his thermoscope (fig. 1.1 (a)). Its concept was fairly simple. A hollow glass ball, filled with air, atop of a hollow glass tube filled with water, the bottom of which was open to a pool of water in which it sat. The pressure of the air in ball pushed down on the water in the tube, keeping it a certain level. When the ball was heated/cooled, the pressure of the air inside would increase/decrease. This would either push the water level down or allow it to rise. This provided a mechanism for visualizing a change in temperature. Of course, without a method to quantify this change, this could hardly be considered a measurement, a shortcoming which was soon to be rectified when Sanctorius added a scale of 8 degrees to the device (fig. 1.1 (b)).[1]

The next major advancement in thermal measurements came from Grand Duke Ferdinand II and Prince Leopold's 'Accademia del Cimento' ('Academy for scientific studies'), as published in their 1667 work 'Saggi di Naturali Esperienze Fatte' ('Essays on Natural Experiments'). One of the topics detailed in this work was their 1654 experiment on what would become renowned as the 'Florentine thermometers'. These thermometers flipped the idea behind the thermoscope on its head. Instead of heating or cooling a pocket of gas, these thermometers transferred heat into a liquid, spirit of wine specifically, which was kept in sealed glass tubes (fig. 1.1 (c)). Ferdinand and Leopold distributed these throughout Europe, where they became the standard for thermal measurements.[1] After a few modifications over time (i.e. shape, thickness, liquid volume and type), the modern versions of these thermometers have an accuracy of around 1 K.[4] This style of thermometer is physically limited to a macro scale spatial resolution and a relatively long acquisition time.

[1]The use of 'degrees' for this scale was likely inspired by Galen's concept of '4 degrees of heating' and '4 degrees of cooling', since the oldest known record of this thermometer had a scale of 8 degrees.[1]

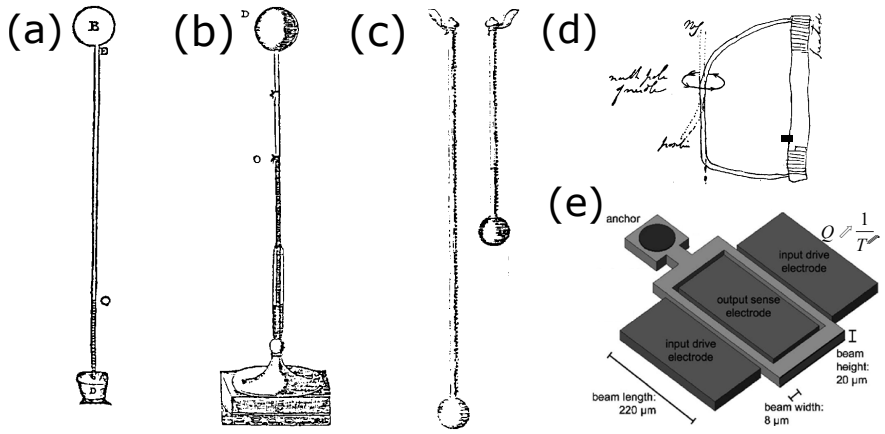

Figure 1.1: (a)A Galilean type thermoscope and (b)a Sanctorius type thermometer, with gas filled bulbs atop liquid filled tubes. Heating(Cooling) the bulb expands(contracts) the gas and the fluid in the tube falls(rises).[1] (c)Florentine thermometers from Plate I of the 'Saggi'. $50°$ and $100°$ versions were produced. In 1829, several of the $50°$ thermometers were shown to have a consistent ice point of $13.5°$.[1] "Reprinted with permission from [1]." (d)Faraday's diary, 21 Oct. 1822 –"Dr. Seebeck's Expt. ... Antimony and brass wire; the bar being heated at one end the north pole of a needle would go round it as... the lower figure... dotted lines represent the state of the wire ... from former experiments".[2] "Reprinted with permission from [2]." (e) The beams of the double-ended tuning fork move between the electrodes with a temperature dependent Q factor.[3]
"Reprinted with permission from [3]."

The world of thermal measurement's next big advancement wouldn't come until 1833, when Faraday recorded the first semi-conductor effect. Working with a sulphuret of silver (silver sulfide), Faraday noticed that when its temperature changed, so did its conducitivity.

> I have lately met with an extraordinary case ... in direct contrast with the influence of heat upon metallic bodies ... when a piece of this sulphuret ... was put between ... terminating pole of voltaic battery ... the conducting power rose rapidly with the heat ... in the manner of a metal ... allowing the heat to fall off, the effects reversed ...
> -*Micheal Faraday*[5]

This effect is exploited in the device known as a thermistor. It has an accuracy on par with the sealed glass thermometer, $\sim$ 1K[6], but can be much smaller in size, with a much shorter acquisition time.

In the early 19^{th} century, Thomas Seebeck was studying Ørsted's work on the relationship

between electrical current and magnetism, leading him, in 1820, to submit a paper discussing his own work on the subject to the 'Berlin Academy of Sciences'. The next year, he was able to show that heating the contact point of two metals in a loop caused changes in their magnetic fields (fig. 1.1 (c)). Five years later, A.C. Becquerel proposed that this 'Seebeck effect' could be used in what would become known as a thermocouple to measure high temperatures.[2]

A more modern approach to measuring temperature came along with the development of micro electromechanical systems (MEMS). MEMS is a general class of devices that, as indicated by their names, are on the micron scale in size. They can be manufactured in a multitude of forms, but one of interest to the topic at hand is that of a set of tuning forks with drive and sensing electrodes, creating a resonating chamber with a spatial resolution on the order of a couple hundred microns (fig. 1.1 (e)). The Q factors these resonating chambers have been found to change with temperature, allowing them to used as thermometers with sensitivities as low as 30 ppm/K, where ppm refers to parts per million variations in frequency. While these MEMS devices are much smaller than the semi-conductor based thermistors or the Seebeck effect based thermocouples, they are still orders of magnitude larger than the minimum size of a diamond color center sensor.

A Diamond color center is an area of a diamond lattice containing some defects. The most popular of these is the NV color center, where one lattice site is occupied by a nitrogen atom and an adjacent site is vacant. Although the fluorescence emitted by this color center has a low contrast between its ZPL and PSB, the fact that it is a spin triplet state has made it useful for ODMR measurements. These measurements are made by hitting the color center with a microwave pulse and measuring the change in the brightness of its fluorescence. When hit with a pulse whose frequency is resonant with either its +1 or -1 spin transitions, its fluorescence will be at it dimmest. These resonant frequencies are uniformly shift along with changes in temperature, allowing thermal measurements to be made with this ODMR.[7][2] The obvious downside to this temperature measurement methodology is the required used of microwave pulses, which can be deleterious to *in vivo* measurements. This malady is absent from all-optical thermal measurements made with

[2]The spacing between these resonant frequencies also changes along with changes in magnetic field.[8] As this fact is outside the scope of this paper, it will not be elucidated any farther.

split-vacancy color centers.

A split-vacancy color center is an area of diamond lattice where two adjacent lattice sites have been vacated, while an impurity sit interstitially between them. Interesting species of these color centers have impurities of non-carbon Group-IV elements (i.e. silicon, germanium, and tin). With 4 valence electrons of the impurity, six unpaired electrons around the vacancies and the tendency for one of the vacancies to trap a free electron, these color centers form an 11 electron system. When phonon-mixing of states is accounted for, this becomes a 4-level system. Once pumped with an optical source, bluer than 600 nm, these color centers fluoresce with a spectrum composed of 4 ZPL's and their accompanying PSB's. Thermal changes in the color center result in changes in the phonic properties of the system, leading to changes in its DWF, peak broadening[9], and peak shifting[10]. Due to the accumulation of these effect, these 4 peak have merged at room temperature, appearing a single spectral peak. Unlike NV spectra, the high contrast between the ZPL's and their PSB's allow these spectra to be analyzed directly, by fitting various distributions to them and recorded the resultant parameters. Since the ZPL broadens homogeneously, it has a Lorentzian distribution, $\mathrm{L}(\lambda)$. In the biological window, where spectra relevant to this thesis were recorded, it has been found that a triple Lorentzian distribution, $\mathrm{L}(\lambda) = \sum_{\mathrm{i}=0}^{2} \mathrm{L_i}(\lambda)$, fits well over the whole peak. The values of the temperature dependent properties of $\mathrm{L}_0(\lambda)$ allow the color center to be utilized as an all-optical quantum thermal sensor.

This type of sensor has a noise-floor, η_{T}, determined by the number of PL photons, N, collected. N is determined by 1.power of the laser pumping it, p, and 2.the acquisition time, Δt, with a lower bound which is inversely proportional to the square root of the product of the two, $\eta_{\mathrm{T}} \propto (\mathrm{p}\Delta\mathrm{t})^{-1/2}$. The downsides in decreasing this noise floor come from both parameters on which is depends. One way of decreasing this noise floor would be to increase the acquisition time. This, of course, would decrease the temporal resolution of measurements. The other way to decrease the noise floor would be to increase the pump power. The downside to increasing the pump power is that doing so increases the heating penalty and, consequently, heating that which is being measured (this can be problematic for *in vivo* measurements).

Unless careful consideration is taken the diamond manufacturing process, NV defects can form in relatively high concentrations unprovoked. Where split-vacancy defects are concerned, diamonds containing these color centers are manufactured in one of two ways. Firstly, for bulk diamonds, ion implantation is a commonly used methodology. In this method, a bulk pure diamond is irradiated with ions of whichever impurity is desired. If the inclination is for localized areas of color centers in an otherwise pure sample a concentrated beam can be used. Another way of achieving this outcome is via the use of a protective mask to isolate implantation regions. Either way, the irradiation not only implants the desired impurities, it also damages the diamond lattice, creating vacancies. Then, the irradiated sample is annealed, letting the lattice rearrange itself as the vacancies migrate toward the heavier implanted impurities, creating the desired color centers.

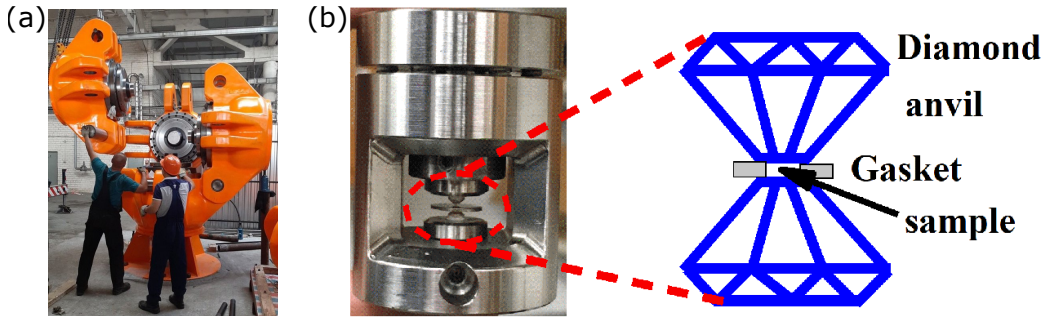

Figure 1.2: (a)The standard industrial HPHT diamond growth chamber utilizes a growth cell containing the diamond seeds, graphite, and a catalyst mixture. The chamber raises the pressure and temperature inside the cell to ≈ 50 GPa and $1,300^\circ$ C.[11] "Reprinted with permission from [11]." (b)This homemade diamond anvil cell (DAC) has a cell chamber in a 100 μm gasket hole and raises the pressure and temperature to 10 GPa and $\approx 400^\circ$ C respectively.[12]"Reprinted with permission from [12]."

Contrarily, smaller diamonds, such as those with sizes on the nanometer scale, can be grown around seeds, such as diamonoid molecules. Diamonoid molecules are essentially engineered molecules containing the atoms needed for the color center. Chemical vapor deposition (CVD) can be used to grow these nanodiamonds. Unfortunately, the plasma utilized by this method tends to destroy the seeds, leaving the final product to be standard carbon diamonds, sans color centers.

The only other viable method is high-pressure high-temperature (HPHT) growth. As the name suggests, HPHT growth involves subjecting the seeds to a pure carbon environment under high-pressures and at high-temperatures. The conventional source of this environment is a machine that is resource intensive financially, spatially, and chronologically, as shown in fig. 1.2 (a). An alternative to this type of apparatus has been found to be a diamond anvil setup. In this setup, parallel facets of two large diamonds are clamped about a gasket with some carbon radicals and seeds inside, as shown in fig. 1.2 (b), which is then heated in a vacuum. This diamond anvil methodology is extremely frugal financially, spatially, and chronologically, with results on par with the traditional HPHT apparatus. These methods can easily be used to grow standard “purer" diamonds; however, when growing around diamonoid, a few considerations must be accounted for. For one, if the temperature is too high, the seed can be destroyed. Also, the growth must be fast enough to encase the impurities before they can be ejected.[13]

Both bulk diamonds diamonds with ion implantation regions and micro-diamonds grown in HPHT environments were used to acquire the ensuing results.

1.2 State of the art

Unlike NV thermometry, split-vacancy thermometry is performed via all-optical processes. As stated previously, NV thermometry measures the change in PL brightness corresponding to applied microwave pulses, due to the temperature dependence of the electron spin resonances of the color center. Split-vacancy thermometry, on the other hand, relies on the contrast between the ZPL and PSB of the color center’s PL spectra to ascertain and exploit the temperature dependence of the shape and location of the spectral peak (more on that later). While the ODMR methodology of NV thermometric measurements are not ideal for *in vivo* measurements, it is still the benchmark for high-resolution, high-sensitivity measurements.

One field that benefits greatly from from diamond color center thermometry is that of neurostimulation. Specifically, neurostimulation via thermogenetics. For both NV and GeV thermometers, the color centers are pumped with a 532 nm laser. Increasing/decreasing the pump power will increase/decrease the temperature of the diamond containing the color centers, which

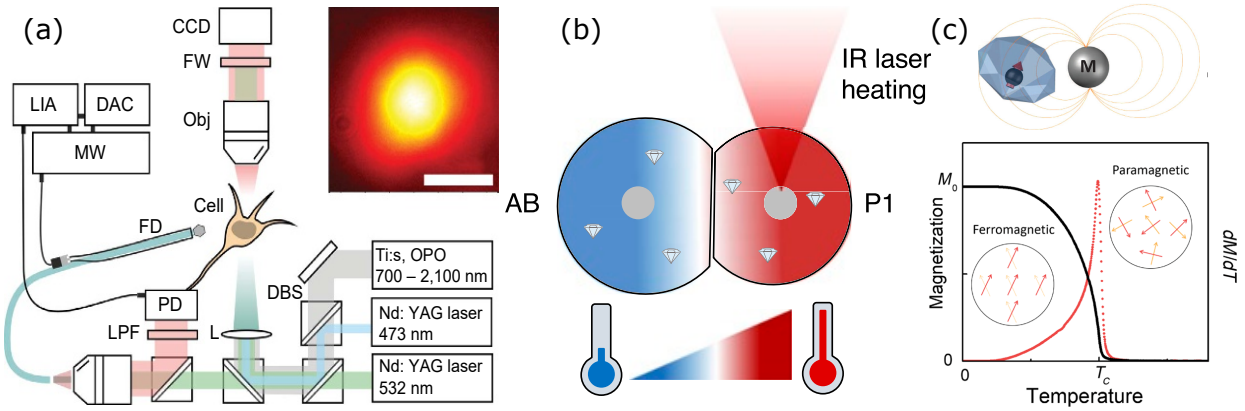

Figure 1.3: (a)A NV probe thermometer (FD) used as a self-referential thermometer for thermogenetic activation of a single neuron (cell).[14] "Reprinted with permission from [14]." (b)NV nanodiamonds used for simultaneous spatially distinct temperature measurements to show the temperature gradient across replicating cells with localized laser heating.[15] "Reprinted with permission from [15]." (c)By placing NV diamond in a magnetic field, knowing the temperature dependence of that field, and knowing the effects of magnetic field on electron spin resonance (ESR) of the NV center, a hybrid thermometer with increased sensitivity was created. [16] "Reprinted with permission from [16]."

allows these types of thermometers to work as self-referential heaters. It is this property which is exploited in thermogenetic experimentation. For example, a diamond thermometer probe is placed in the vicinity of a neuron which expresses thermosensitive receptive potential (TRP) cation channels. As the name suggests, when a TRP cation channel is heated, it opens and allows the neuron to fire. Due to the falloff rate of the heat radiated by the diamond, this thermogenetic approach can address a single neuron, as opposed to previous optogenetic approaches with larger areas of effect. An experiment demonstrating this was conducted with mouse neurons expressing TRPA1 channels, which are normally found in snakes (see fig 1.3 (a)). The heater was a NV diamond fiber probe (FP). The beam from a Nd:YAG laser was coupled into one end of a fiber, which had a NV diamond attached to the other end. This allowed the laser to pump the color centers, without flooding the region with the light. Also, the fiber collects the PL emitted from the diamond allowing it to be collected by the photodiode. In order to facilitate the the ODMR, a wire, carrying microwave pulses, ran the length of the fiber and looped around the diamond. Once the pump power was increased sufficiently to heat the diamond enough to cause the neuron to fire, it was

reduced, allowing the temperature to abate and the channel to close. This cycle was shown to be able to repeatedly fire specifically target neurons. [14] Although this experiment was performed with a NV-probe utilizing ODMR measurements, it should also be able to be accomplished with a GeV fiber probe using all-optical thermometry. Doing so would allow this type of experiment to be performed *in vivo* , without need for the biologically damaging microwave signals.

Another field in which diamond thermometry is useful is in cellular biology. Since the minimum size of a color center containing diamond is much smaller than a cell and diamonds are non-toxic, a cell can be flooded with them allowing them to provide a thermal profile of the cell while it undertakes various processes. This approach was used in an experiment performed on caenerhabditis elegans (roundworm) embryos.[15] As illustrated in fig. 1.3 (b), roundworm embryos were implanted with NV nanodiamonds and cell division was induced via localized infrared (IR) heating. In order to maximize cell division rates, ODMR measurements on the nanodiamonds were used to control the IR heating in order to maintain the proper thermal gradient across the embryos. The simultaneous measurements of several nanodiamonds necessary for this experiment was able to be accomplished due to the simple fluorescence brightness measurements needed for the ODMR process. Although, the previously discussed methods of measuring the peak shift, peak broadening, or change in amplitude of the fluorescence peak of a single split-vacancy color center, does not lend itself to simultaneous measurements that would need to be made if this type of experiment were attempted with them, there is another methodology that would work. The split-spectrum intensity integration technique (detailed later) could be used to preform the measurements needed for this type of experiment. Briefly, this technique exploits the temperature dependence of the color center's DWF and its effects on the fluorescence peak's ZPL and PSB, allowing temperature measurements to be made without individual peak analyses.

In NV thermometry, direct thermometric measurements are known to have sensitivities of several $\mathrm{mK}/\sqrt{\mathrm{Hz}}$; however, better sensitivities have been demonstrated via hybrid thermometry. With direct thermometric measurements, the zero-field splitting, D, is measured through ODMR. In hybrid thermometry, a NV nanodiamond is placed in the next to a magnetic nanoparticle (MNP),

whose magnetic field strength is temperature dependent (fig. 1.3 (c)). With this setup, ODMR is used to measure the effect of the magnetic field on the transition frequencies ($m_s = 0 \leftrightarrow m_s = \pm 1$) of the NV spins. With the MNP designed with known temperature dependence of their magnetic fields, this ODMR measurement of said magnetic field is also a temperature measurement. This methodology has been shown to achieve sensitivities in the sub-mk$/\sqrt{\text{Hz}}$ range.[16] Of course these measurements still have the setbacks of ODMR. Also, the temperature dependence of the sensitivity must be considered. For these MNP's, the best sensitivity is near its Curie point, with an optimal working range on the order of 20 K. In opposition, GeV thermometry maintains its sensitivity throughout the biological window (293-333 K).

2. BACKGROUND

2.1 Motivation

The following experiments develop methods of performing all-optical quantum thermometry by examining the behaviors of split-vacancy diamond color center fluorescence peaks in response to thermal stimuli, namely the precision and sensitivity limits of measurements to line shift, spectral broadening, peak amplitude changes, and changes to the peak's DWF. Experiments using fiber probes and split-spectrum intensity integration will be detailed to demonstrate applicability in high-spatial resolution thermometry and bolometry, while open-air thermometric measurements will identify the limitations of these measurements.

2.2 Statement of problem

Diamond based thermometry is attractive for *in vivo* measurements, due to the facts that they are chemically inert, nearly non-toxic and can achieve a high spatial resolution. Its commonplace to use diamonds with NV color centers for these measurements; however, their drawback is that they require microwave pulses to perform them. This weakness is eliminated with split vacancy thermometry. Unfortunately, this solution introduces another limitation in the trade off between sensitivity and heating, especially in Group-IV color centers. This comes from the fact that the pump beam must be bluer than the spectral peak (e.g example a 532 nm Nd:YAG to get a GeV to fluoresce at 601 nm), which heats the diamond. Due to the fact that sensitivity is dependent on photon count, coupled with the fact that increased pump power increases the photon count of the fluorescence, split-vacancy color center thermometry must sacrifice a heating penalty for improved sensitivity. For example, in an experiment detailed later in this paper, measurements with GeV's pumped at a relatively high 50 mW, were able to achieve a high sensitivity, $\eta_{\mathrm{T}} \approx 0.6$ mK$/\sqrt{\mathrm{Hz}}$, but suffered from a heating penalty of around 10 K. Induced heating of this nature can be prohibitive to *in vivo* measurements. Also the possibility of near-IR thermometry with NiV's could lead to thermal measurements being made through much thicker biological materials.

2.3 Tools

2.3.1 Group-IV split-vacancy color centers as eleven electron systems

When two adjacent diamond lattice sites are vacant, there are six unpaired valence electrons. The addition of an Group-IV atom, interstitially between those two vacancies, adds another four electrons to the color center. The vacancy sites are now surrounded by unpaired valance electrons and can trap a free electron in a superposition between the two vacancies. This configuration is a split-vacancy color center with a charge of -1. Under proper circumstances, the trapped free electron can be ejected, or another electron can be captured, leading to a plethora of potential charge states.[17] . An example of this is shown in fig. 2.1 (a) with a germanium as the interstitial atom and 1 captured electron. Considering a XV^{-1} state, where $X \in \{Si, Ge, Sn, Pb\}$. With these eleven unpaired electrons, a color center of this type is analogous to a sodium atom. A sodium atom has one valence electron in the 3s orbital shell, allowing for 2 possible ground states $^2S_{1/2}$(spin up/down,m_1=0) and 6 excited states, $^2P_{3/2}$ (spin up/down, $m_1 = \pm 1$) and $^2P_{1/2}$ (spin up/down, $m_1 = 0$).

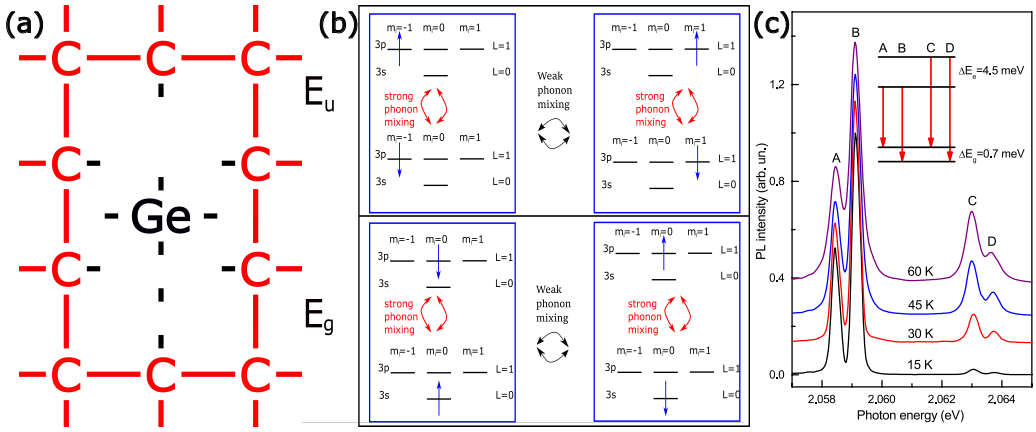

Figure 2.1: (a)Germanium between two diamond vacancies forms an 11 e^{-1} system. (b)Weak and strong phonon mixing reduce the number of ground and excited states of the eleven electron system. (c)Group-IV split vacancy spectra at various temperatures.[18] "Reprinted with permission from [18]."

When taken in isolation, this electron configuration suggests 8 possible states for the electron to be in; but that is there is a difference between the sodium atom and a Group IV color color center that has yet to be accounted for. That difference is the fact that the color center is, intrinsically, bound to the diamond lattice. This fact demands the consideration of phonon mixing. Such as the strong phonon mixing between the $^2S_{1/2}$ spin up(spin down) and $^2P_{1/2}$ spin up(spin down) states, as well as weak mixing between those states. Also, there is strong mixing between $^2P_{3/2}$, $m_1 = -1$ ($m_1 = 1$) spin up and down states. There is weak mixing between those states as well. As shown in fig. 2.1 (b), these mixing relations drop our 8 state system to a 4 state system, as demonstrated in low temperature spectroscopy as 4 ZPL's with their accompanying PSB's (fig. 2.1 (C)).

2.3.2 Temperature dependent behaviors of split-vacancy color center spectral properties

Due to electron–phonon interactions, various properties of the fluorescence of the color center have been shown to predictably vary with temperature. These properties include central wavelength, peak width, amplitude and DWF.

2.3.2.1 Line shift

As laid out in the paper '*Electron–phonon processes of the silicon-vacancy centre in diamond*', published by Kay Jahnke et al in "New Journal of Physics", the spin–orbit splitting shifts like:

$$\frac{1}{2}\left(\overline{\delta E_-} + \overline{\delta E_+}\right) = -2\hbar\chi\rho \int_0^{\Omega} \frac{2e^{\frac{\hbar\omega}{k_B T}}\left(e^{\frac{2\hbar\omega}{k_B T}} + 3\right)}{\left(e^{\frac{\hbar\omega}{k_B T}} - 1\right)\left(e^{\frac{1\hbar\omega}{k_B T}} + 1\right)}\omega^2 d\omega$$
$$\propto T^3$$

where χ and ρ are proportionality constants for the phonon interaction frequency, $\chi_k(\omega)$, and the density of modes, $\rho(\omega)$, respectively.[19]

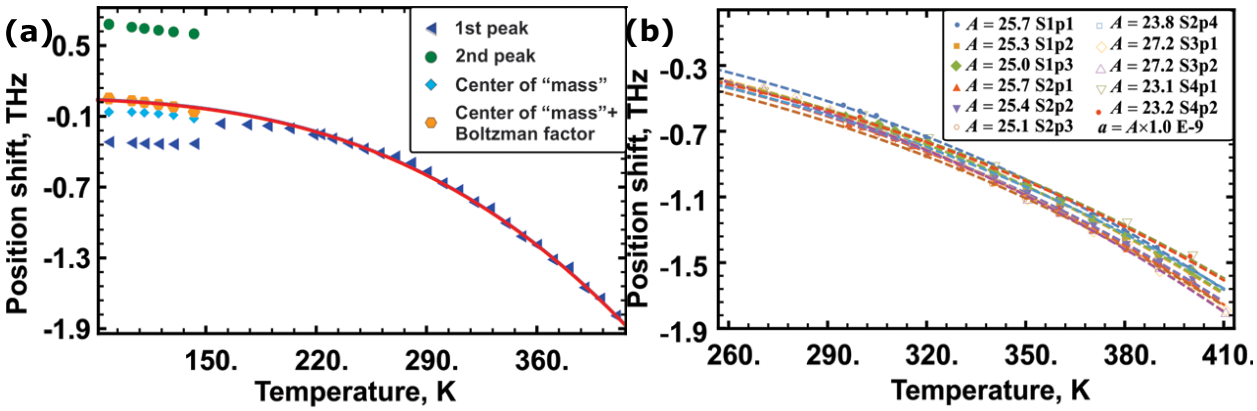

Figure 2.2: T^3 dependence of the central wavelength shift of GeV fluorescence, (a), is shown to be the same across multiple samples with various vertical shifts, (b).[20] "Reprinted with permission from [20]."

The behavior of this shift is expressed spectrally as as the central wavelength of the fluorescence becoming redder with a T^3 dependence, see fig. 2.2 (a). When different samples were interrogated, the same T^3 behavior was detected, but each one different y-intercepts.

2.3.2.2 Peak broadening

In the same Jahnke paper, the relaxation rate, due to electron–phonon interactions go like:

$$\gamma_{d-/+} \approx 2\pi \left(\hbar \Delta \chi \rho\right)^2 \int_0^\infty \mathrm{n}\left(\omega, \mathrm{T}\right) \left(\mathrm{n}\left(\omega, \mathrm{T}\right) + 1\right) \omega^2 \mathrm{d}\omega$$
$$= \frac{2\pi^3}{3\hbar} \left(\Delta \chi \rho\right)^2 {k_B}^2 \mathrm{T}^3$$

Here, Δ refers to spin-orbit splitting, $\mathrm{n}\left(\omega, \mathrm{T}\right)$ is the occupation function, and, again, there is a T^3 dependency.[19]

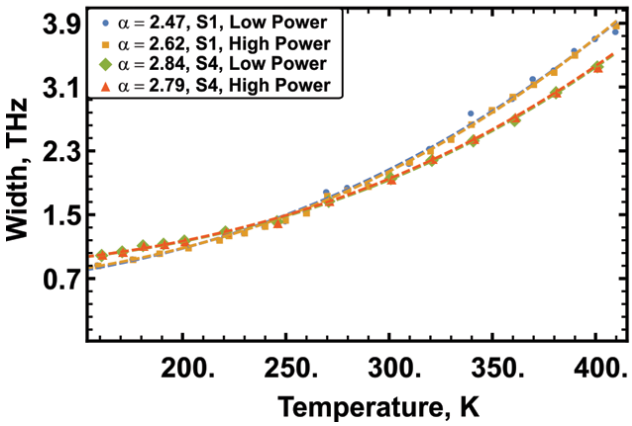

Figure 2.3: T^3 dependence of peak broadening.[20] "Reprinted with permission from [20]."

Since the relaxation rate determines spectral peak width, the experimental results showing a T^3 dependence of peak broadening is expected.[20]

Linear approximation:

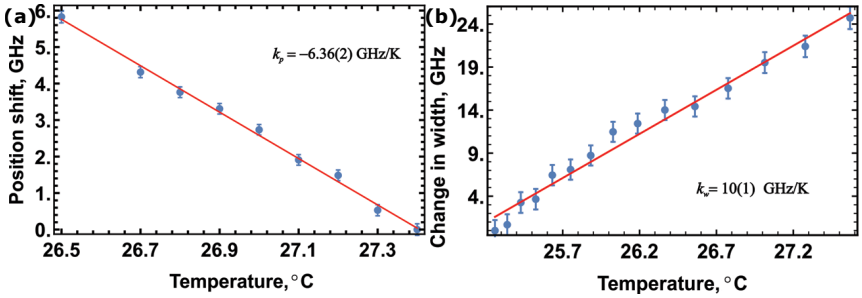

Figure 2.4: Although it has been shown that line shifts and peak broadening have T^3 dependence over a wide range of temperatures; a linear approximation provides accurate relationships to line shifts, (a), and peak broadening, (b), over short temperature ranges about the biological window. [20] "Reprinted with permission from [20]."

2.3.2.3 Temperature dependence of peak amplitude

The ZPL of the fluorescence spectrum produced by a sample of GeV color centers is generated by purely electronic transitions. This means that it broadens homogeneously, giving it a Lorentzian

profile, per example:

$$\mathrm{L}\left(\lambda\right) = \frac{\mathrm{A}\gamma}{\pi\left[\left(\lambda - \lambda_{\mathrm{c}}\right)^{2} + \gamma^{2}\right]}$$

with peak width, γ, and central wavelength,λ_{c}. Now consider a peak, $\mathrm{L}_{1}\left(\lambda\right)$ at temperature T_{1}, with central wavelength at $\lambda_{\mathrm{c}1}$ and width of γ_{1}. Now consider the peak changing, $\mathrm{L}_{2}\left(\lambda\right)$, due to a change in temperature, $\mathrm{T}_{1} \rightarrow \mathrm{T}_{2}$, with a corresponding line shift, $\lambda_{\mathrm{c}1} \rightarrow \lambda_{\mathrm{c}2}$ and peak broadening, $\gamma_{1} \rightarrow \gamma_{2}$:

$$\mathrm{L}_{1}\left(\lambda\right) = \frac{\mathrm{A}_{1}\gamma_{1}}{\pi\left[\left(\lambda - \lambda_{\mathrm{c}1}\right)^{2} + {\gamma_{1}}^{2}\right]} \rightarrow \mathrm{L}_{2}\left(\lambda\right) = \frac{\mathrm{A}_{2}\gamma_{2}}{\pi\left[\left(\lambda - \lambda_{\mathrm{c}2}\right)^{2} + {\gamma_{2}}^{2}\right]}$$

Due to electron–phonon processes, a rise in the temperature of a GeV color center actually decreases the total energy in the ZPL. This means that the effects that will be demonstrated presently will be greater than what is shown. With that in mind, assuming conservation of energy, the integral over both of these spectra should be equal. i.e.

$$\begin{gathered}
\int_{\mathbb{R}} \mathrm{L}_{1}\left(\lambda\right) = \int_{\mathbb{R}} \mathrm{L}_{2}\left(\lambda\right) \\
\frac{\mathrm{A}_{1}}{\pi}\arctan\left(\mathrm{u}\right)\Big|_{-\infty}^{\infty} = \frac{\mathrm{A}_{2}}{\pi}\arctan\left(\mathrm{u}\right)\Big|_{-\infty}^{\infty} \\
\frac{\mathrm{A}_{1}}{\pi}\pi = \frac{\mathrm{A}_{2}}{\pi}\pi = \mathrm{A}
\end{gathered}$$

It is evident that the value of a Lorentzian is maximized at $\lambda = \lambda_{\mathrm{c}}$, i.e.

$$\mathrm{L}_{1(2)\mathrm{max}}\left(\lambda=\lambda_{\mathrm{c}1(2)}\right)=\frac{\mathrm{A}}{\pi\gamma_{1(2)}}$$

$$\therefore\frac{\mathrm{L}_{1\mathrm{max}}}{\mathrm{L}_{2\mathrm{max}}}=\frac{\gamma_2}{\gamma_1}$$

Since this treatise concerns an increase in temperature, and literature and experiment indicates that this leads to an increase in peak width, it holds that $\gamma_2>\gamma_1$.

$$\therefore\frac{\gamma_2}{\gamma_1}>1$$

$$\frac{\mathrm{L}_{1\mathrm{max}}}{\mathrm{L}_{2\mathrm{max}}}>1$$

$$\mathrm{L}_{1\mathrm{max}}>\mathrm{L}_{2\mathrm{max}}$$

showing that, even in the unobtainable optimum circumstances, peak amplitude decreases as temperature increases. As previously stated, this effect is enhanced due to lose of energy due to electron–phonon interactions.

2.3.2.4 Temperature dependence of DWF

The DWF is chiefly used to describe the diminishment of x-ray/coherent neutron scattering in a crystal due to thermal motion of atoms about their lattice sites. Given by:

$$\mathrm{B}=\frac{4\pi^2}{\mathrm{m}}\int_0^{\omega_{\mathrm{m}}}\coth\left(\frac{\hbar\omega}{2\mathrm{k_B T}}\right)\left[\frac{\mathrm{g}\left(\omega\right)}{\omega}\right]\mathrm{d}\omega$$

in which ω_{m} is the maximum phonon frequency and m is the mass of the atom. It should also be noted that the DWF of a crystal is also dependent on temperature, T, and phonon density of states, $\mathrm{g}\left(\omega\right)$.[21]

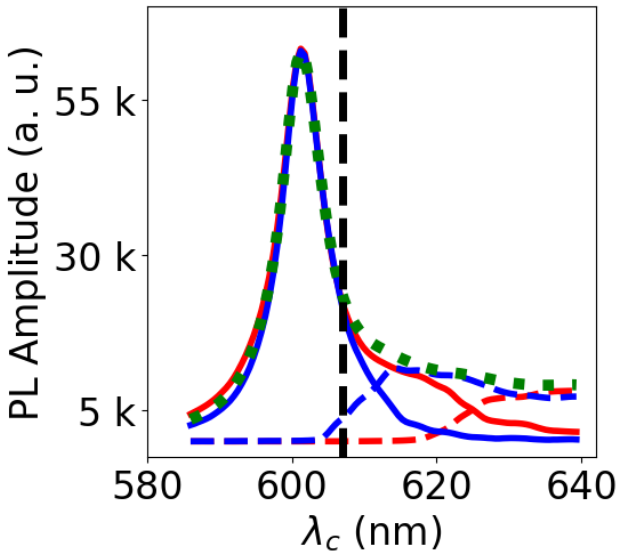

Figure 2.5: Spectral peak ZPL and PSB deconstruction.

Since the fluorescence peak of a split-vacancy color center is a convolution of a ZPL and a PSB, and the DWF is a function of temperature and phonon density of states, it is argued that the percentage of the total spectral peak fluorescence that is contributed by the ZPL (the solid blue line in fig. 2.5) is determined by the DWF. For this reason, the measurement of said percentage will be referred to as the color center's DWF. This measurement will be made in two ways. One way is through pure numerical integration of recorded spectra. In this method, all of the spectra bluer than a splitting wavelength (black dashed line in fig. 2.5) is numerically integrated and divided by the integration of the wavelengths redder than the splitting wavelength. The second way this will be measured is through split-spectrum intensity integration. Put simply, with a more complete description to come, a dichroic mirror (DM) separates the redder photons from the bluer ones and integrates each portion individually via a charge-coupled device (CCD) camera.

2.3.2.5 Wrap up

It has been demonstrated that a GeV color centers emit a fluorescence peak with temperature dependent line shift, peak width, peak amplitude, and DWF. The next section will detail the experiments utilizing measurements of these properties to produce all-optical thermal sensors.

3. RESULTS

Interrogation of temperature dependent properties of split-vacancy color centers in diamond has been performed via 3 general modalities: fiber probe spectroscopy, split-spectrum intensity integration, and open-air spectroscopy. Two experiments were performed with fiber probe spectroscopy.[10][9] In '*Fiber-Optic Quantum Thermometry with Germanium-Vacancy Centers in Diamond*', a probe was constructed with a bulk diamond containing ion implantation regions of GeV color centers. In its execution, peak broadening and line shifting measurements were used to create a 1-dimensional thermal image.[10] '*Photonic-Crystal-Fiber Quantum Probes for High-Resolution Thermal Imaging*' focused on spatial resolution by employing a microdiamond containing GeV's. Temperature measurements calculated from line shifting were used to produce a 2-dimensional thermal image.[9] The experiment performed by means of split-spectrum intensity integration used the thermal dependence of the DWF to measure the temperatures of several spatially distributed GeV microdiamonds simultaneously to construct a 2-dimensional thermal image. Then, the open air modality was employed with 1.a GeV diamond, establishing the noise floor of measurements and their links to heat penalties, and 2.NiV diamond color centers, to push toward near-IR thermometry.

As stated earlier, spectral analysis on the GeV fluorescence peaks was performed by the extraction of parameters found by the fitting the recorded spectra with triple Lorentzian distributions, $\mathrm{L}(\lambda) = \sum_{\mathrm{i}=0}^{2} \mathrm{L_i}(\lambda)$, where

$$\mathrm{L_i}(\lambda) = \frac{\mathrm{A_i}\gamma_\mathrm{i}}{\pi\left[(\lambda - \lambda_\mathrm{i})^2 + {\gamma_\mathrm{i}}^2\right]}$$

, with γ_i, λ_i, and $\mathrm{A_i}$ being the peak width, central wavelength, and amplitude of the i^{th} Lorentzian, respectively. Since the behaviors of interest concern the ZPL, it is the parameters of L_0 that are of interest.

3.1 Fiber probe spectroscopy

For the 2 experiments conducted with this technique, fiber probes were constructed by, firstly, attaching the core of one end of an optical fiber to a diamond containing GeV's. In '*Fiber-Optic Quantum Thermometry with Germanium-Vacancy Centers in Diamond*', a standard fiber with a 50 μm core was attached to the GeV implantation region of a bulk (2 mm by 2 mm by 1 mm) diamond.[10] Then, for '*Photonic-Crystal-Fiber Quantum Probes for High-Resolution Thermal Imaging*' a 5 μm GeV was diamond attached to the 5 μm core of a photonic crystal fiber (PCF). The PCF was used because it was able to achieve a small enough core size with a high enough numerical aperture to collect all the modes of the diamond's fluorescence.[9] Except for the fiber and diamond components, both of these experiments utilized the same components in the same configuration. Once the fibers had their diamonds attached to one end, the second-harmonic of a 532 nm Nd:YAG laser was coupled into the opposing ends of the fibers, where it then propagated through the fibers, pumping the GeV's. The diamonds' fluorescences were then collected by their respective fibers, counter-propagating back to the ends into which the laser was coupled. Upon leaving the fibers, the fluorescence signals were filtered from the pump light, via a DM, and collected by spectrometers. See figures 3.1 (a) and 3.3 (a).

For the bulk diamond probe, the probe tip was placed in direct physical contact with a heating system which consisted of a copper plate, a thermistor, a thermo-electric cooler (TEC), and a proportional-integral-derivative (PID) controller. Once the copper plate was heated to a desired temperature, the fluorescence from the probe was collected and analyzed. This was repeated for temperatures ranging from 20° C to 50° C. The central wavelengths and peak widths were then calculated for measurements at each temperature and linear fits were found, creating calibration curves shown in fig. 3.1 (b). These calibration curves were found to have slopes of 0.013 nm/K (width) and 0.008 nm/K (central wavelength), in accordance with the literature.

The probe was then translated across a heated 120 μm copper wire in 25 μm steps, with spectra recorded at each step (fig. 3.2 (a)). Analyses of the recorded spectra were then compared with the established calibration curves to determine the temperature of the probe tip at each step in

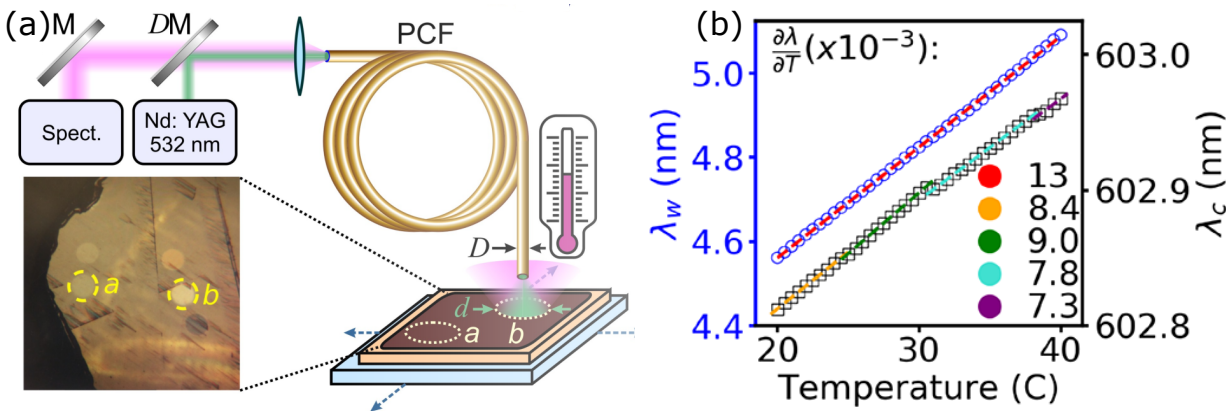

Figure 3.1: (a)An optical fiber attached to a GeV implantation region is optically pumped and the fluorescence is sent to a spectrometer.[10]. (b)Spectra were recorded and analyzed at various temperatures, creating calibration curves for peak width (λ_W) and central wavelength (λ_c).[10] "Reprinted with permission from [10]."

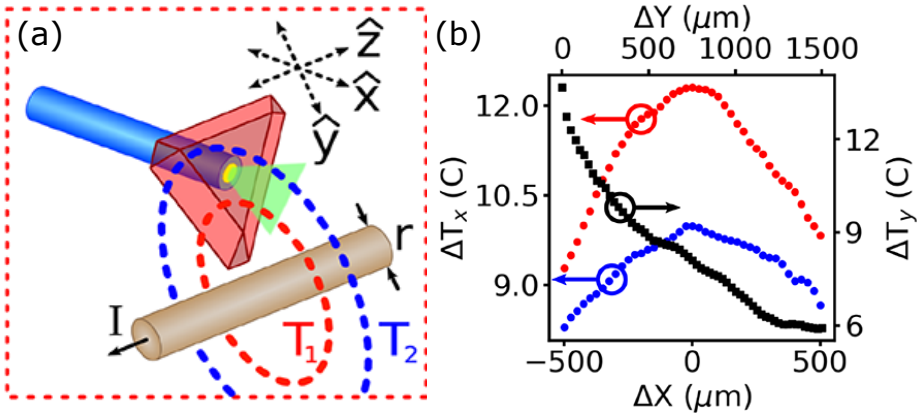

Figure 3.2: (a)The tip of the fiber probe was moved across a heated wire, with spectra being recorded at 25 μm increments.[10] (b)Thermal images of heated copper wire, with one image along the y-axis (black squares) and two images along x-axis (red and blue circles), each at its own constant y-coordinate.[10] "Reprinted with permission from [10]."

the translation. It was translated once along the y-axis (black squares in fig. 3.2 (b)) and twice along the x-axis (blue and red circles in fig. 3.2 (b)) creating 3 1-dimensional thermal images of heat dissipation around the wire with a spatial resolution of 25 μm. This experiment was able to achieve sensitivities better than 20 mK/$\sqrt{\text{Hz}}$.[10]

Since the whole of the bulk diamond was larger than the fiber to which it was attached, heating

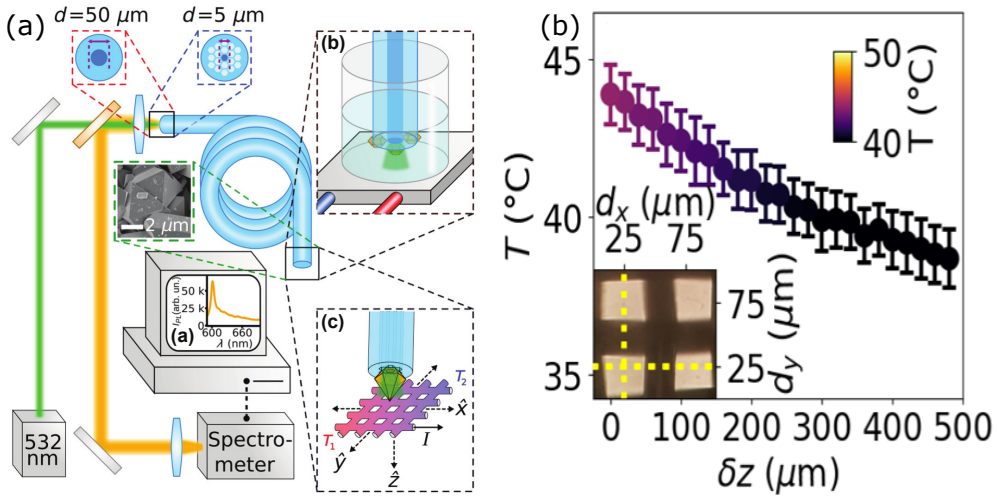

Figure 3.3: (a)A microdiamond is attached to the 5μm core of the PCF and scanned over a heated wire grid while recording spectra at 5μm steps. The analyzed spectra was used to create a 2D-thermal image.[9] (b)Z-axis temperature dependence of probe with recorded convection current fluctuations on the order of $\pm$ 1K. Inset is an optical image of a section of the wire grid.[9] "Reprinted with permission from [9]."

it by placing it on the heated copper slab was trivial. The microdiamond, alternately, was similar in size to the PCF core to which it was attached, prohibiting the employ of the same method. Instead, the motor from an optical disk drive was used to create a stirring mechanism. This stirring mechanism was then used to stabilize the temperature in a water bath, heated with the same PID, TEC, and thermistor as used prior. The microdiamond probe was then placed in this bath and spectra were recorded at various temperatures, ranging from 25° C to 50° C. This data was then analyzed, extracting the central wavelength for each spectrum. In agreement with the literature, a calibration curve with a slope of 0.0078 nm/K and a sensitivity of 20 mK/$\sqrt{\text{Hz}}$ were calculated.

The probe trip was then placed 20 μm from a heated wire mesh, consisting of 30 μm wires and a 60 μm pitch. Spectra were then recorded, at each step, as the probe was translated away from the mesh in 20 μm steps. The temperature distribution along this z-axis is shown in fig. 3.3 (b). At the first 3 steps, z=20 μm , 40 μm , and 60 μm , the probe was then raster scanned of a 500 μm by 500 μm area in 5 μm steps, with spectra recorded at each step. Using the previously calculated calibration curve, temperature data were extracted from location and, utilizing Fourier-filtering, thermal images were constructed of each scan. The image constructed while scanning at z=20 μm is shown in fig. 3.4 (a). Fig. 3.4 (b) shows the trace of the inset of that image along the locations indicated (yellow dotted lines) in fig. 3.3 (b). These traces show the thermal changes around the features in the inset. Also, the trace along the black dotted line in fig. 3.4 (a) shows the uneven heating in the grid wires (see fig. 3.4 (c)).

These experiments demonstrated the ability use GeV diamonds to perform all-optical thermometry with high sensitivity, high precision, and high spatial specificity, via measurements of fluorescence broadening and line-shifting.

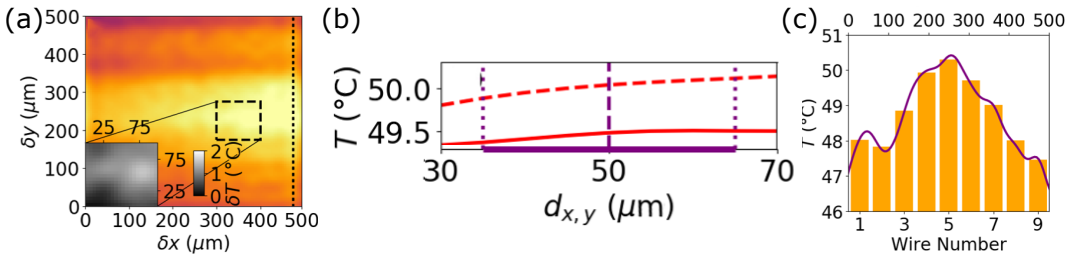

Figure 3.4: (a)Fourier-filter thermal image of heated wire grid with probe at a distance of 20 μm.[9] (b)Traces the inset of (a) along yellow traces in the inset in fig. 3.3(b), with purple dashed and dotted lines representing the center and edges, respectively, of the wires depicted in the inset of fig. 3.3(b).[9] (C)Purple trace of the black dotted line in (a), showing wire-to-wire thermal variations indicating uneven current along the y-axis.[9] "Reprinted with permission from [9]."

3.2 Split-spectrum intensity integration

Working with the thermal dependence of the DWF of a split-vacancy color center, along with the assertion that the percentage of the total fluorescence emitted by said color center in its ZPL, a novel method of all-optical GeV thermometry was developed, which did not require spectroscopic measurements. The technique for this measurement modality begins by splitting the fluorescence spectrum into its ZPL and PSB components. Then, the intensities of each of these components are integrated and compared. The idea behind this integration is that an each component is imaged on a CCD camera and the number of counts of each pixel of the image, when summed over all pixels, is the integral of the intensity of that component of the spectrum. The chief benefits of this method, over the previously discussed methods, are twofold. First, there is no process of recording a spectra, fitting a distribution function to it, extracting the parameters of that fit, and ascertaining a temperature measurement from that. Instead, this method requires simply recording an image from the CCD and summing up the counts. Secondly, whereas the previous method could only record the temperature of a field by measuring one point at a time, losing temporal resolution in the measurement of the whole field. Conversely, this method can use multiple diamonds, measuring them all simultaneously, greatly improving temporal resolution.

Measurements of this type were achieved by first pumping a field of GeV microdiamonds with the Nd:YAG laser. Then, an objective (Obj.) collected the emitted fluorescence and directed it to a DM, which split the ZPL fluorescence from the PSB fluorescence by reflecting the wavelengths shorter than a critical wavelength and transmitting wavelengths longer than that critical wavelength. The reflected and transmitted components of the fluorescence were then simultaneously imaged abreast on the CCD, as shown on fig. 3.5 (a). Now, consider the short wavelength image. For each diamond in that image, the number of counts for each pixel occupied by that diamond are summed over, giving the total intensities for the ZPL's of all the diamonds in the field. This same summation performed on the long wavelength image gives the total intensities for the PSB's of all the diamonds in the field. The ratios of these calculations gives the DWF measurements for each diamond in the field. Since this method allows for multiple, spatially distinct diamonds

to be measured simultaneously, instantaneously generating 2-dimensional thermal images with a temporal resolution limited only by the exposure and processing times for each image.

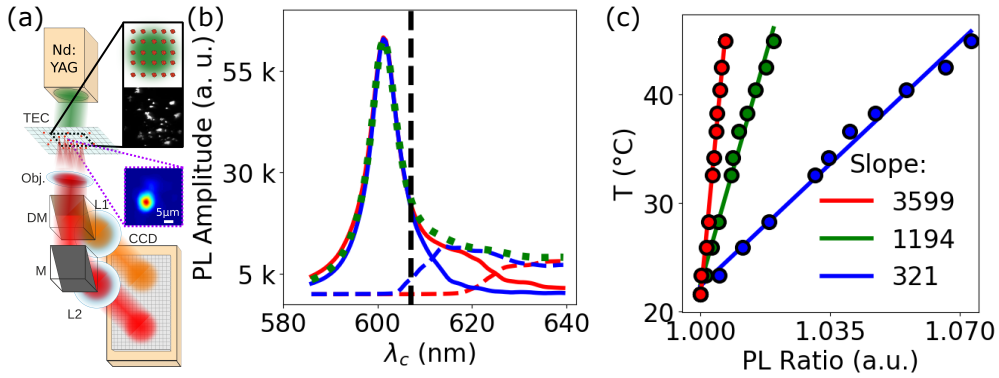

Figure 3.5: (a)A field of diamonds are pumped and their fluorescence is collected by the objective (Obj). Then, the DM separates the short and long wavelengths and images them, juxtaposed, on the CCD. (b)With the full spectrum, the green dotted trace, split at one critical wavelength, the blue solid line shows what portion of the fluorescence is reflected off of the DM, while the blue dashed line shows the fluorescence transmitted through the DM. Similarly, the solid and dashed red lines show the same thing for a separate critical wavelength. The black dashed line shows the absolute angle cutoff used in numerical calculations based on recorded spectra. (c)Thermal response of fluorescence ratio for critical points at 610 nm (blue), 625 nm (red), and 607 nm (green), demonstrating an optimal response of ~ 3600 K.

To determine the optimal properties of the DM, 2 different critical wavelengths were tested. Results using critical wavelengths at 610 nm and 625 nm are shown in fig. 3.5 (b) as red and blue traces, respectively. Also, a critical wavelength was calculated mathematically by numerical integration of recorded spectra. This critical wavelength was calculated to occur at 607 nm (vertical black dashed line in fig. 3.5 (b)). The thermal response (precision) for these three critical points was measured by heating the diamonds with the PID,TEC, thermistor setup used previously and recording images and spectra at various temperatures. The highest precision was found with the 625 nm critical wavelength, as shown in fig. 3.5 (c).

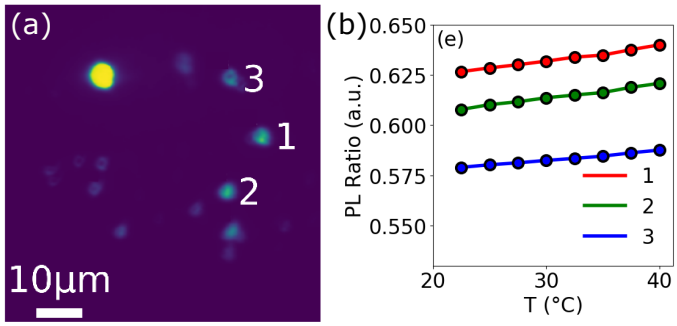

Figure 3.6: (a)Field of fluorescing diamonds acting as thermal image pixels. (b)Thermal response from fluorescent ratios cut at the 625 nm critical point, for the three pixels in (a), were found to have the same slope.

With the optimal critical wavelength determined, a field of GeV microdiamonds (fig. 3.6 (a)) were pumped with the Nd:YAG laser and imaged at various temperatures, demonstrating fluorescence ratios of similar precisions (fig. 3.6 (b)). A sensitivity of 130 $\mathrm{mK}/\sqrt{\mathrm{Hz}}$ was calculated, as a resultant from a noise floor of 1 K per frame at a frame rate of 60 Hz.

Next, to demonstrate the ability of this method to perform thermal mapping, another field of GeV microdiamonds (fig. 3.7 (a)) was heated with the Gaussian profile of a 635 nm laser. Treating each diamond as a thermal pixel in a 2 dimensional array, the power distribution of the beam was modelled as it would spread across the array (fig. 3.7 (c)). The thermal map was compared to the numerical power distribution model, determining the power to heat ratio for each pixel. The power of the heating laser was then varied, as measurements were taken to find the slope for applied power as a function of pixel temperature. This slope was then used to find P_{abs}, which was then used to reconstruct the beam profile in fig. 3.7 (b), as shown in fig. 3.7 (d).

This experiment shows a viable form of biologically friendly thermal imaging, with pixel sizes limited only by the size of the diamonds used.

3.3 Open-air spectroscopy

The fiber probe modality offers unsurpassed mobility. Once constructed, the probe tip can be easily placed nearly anywhere a temperature measurement needs to be taken. Its main drawback

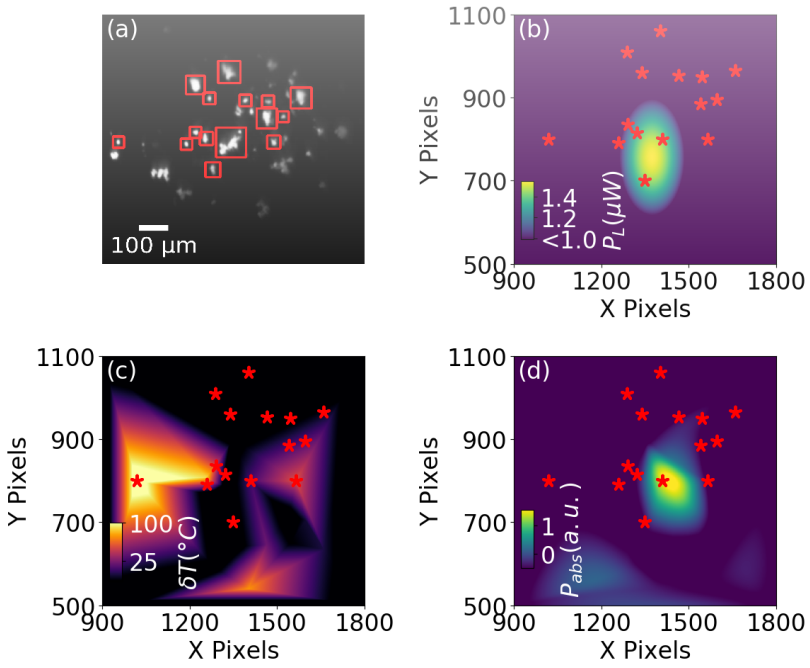

Figure 3.7: (a)Field of diamond thermal pixels (red boxes) used in imaging. (b)Numerical model of 25 mW focal spot of 635 nm diode laser with a Gaussian beam profile. Red stars represent thermal pixel locations. (c)Thermal map of thermal measurements of pixels in (a) under heating by the laser modelled in (b). (d)Power normalized by absorbance (P_{abs}) spatial profile interpolated from thermal map (c).

is the fact that, by its very nature, it only collects a small percentage of the total fluorescence emitted by the color centers. Since the standard deviation of the temperature readout is inversely proportional to the square root of the number of photons collected (i.e. $\sigma_T \propto N^{-1/2}$) at the shot-noise-floor level, the low collection efficiency of the fiber probe directly leads to a decrease in measurement sensitivity. This third technique sacrifices the mobility of the fiber probe, but enjoys a much higher collection efficiency, increasing the sensitivity of the measurements.

The general mechanisms utilized by this method are nearly identical to the fiber probe method. The setups would be indistinguishable form one another if M3 and Obj were replaced with a fiber (fig. 3.8 (a)). As usual, in analyzing recorded spectra, a triple Lorentzian was fit to the peak (fig. 3.8 (b)), with $L_0(\lambda)$ indicating the properties of the GeV ZPL, while $L_1(\lambda) + L_2(\lambda)$ indicating the properties of the PSB. The central wavelengths, peak widths, and amplitudes were measured in the same way as they were in the fiber probe experiments, while the DWF's were measured by

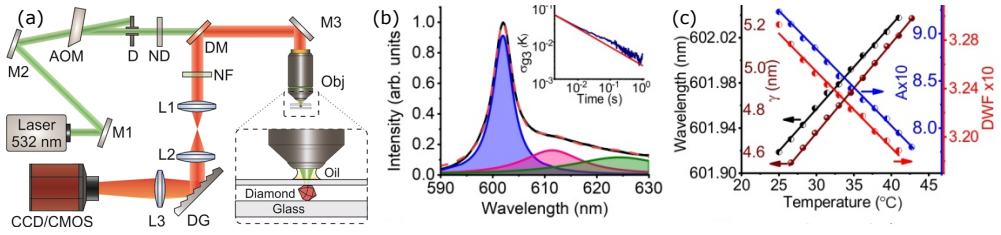

Figure 3.8: (a)The setup for this modality has a CW laser with 2 totally reflective mirrors (M1 and M2), an acousto-optic modulator (AOM) and an iris (D), which allows the laser to be pulsed in concert with acquisition times. The laser then travels through a neutral density filter (ND) and dichroic mirror (DM), before hitting another mirror (M3) and coupling into the objective (Obj) above the GeV diamond. Obj collects the PL, reflecting off M3 and DM, to be collected by the spectrometer [lenses (L1, L2, and L3), a diffraction grating (DG), and a camera]. (b)The overall GeV PL spectrum (black), the fitted triple Lorentzian (red dashed), and the decomposed Lorentzians (blue, pink, and green shaded). (c)Calibration curves for λ_0 (black), γ_0 (brown), A_0 (blue), and DWF (red) as functions of temperature for PL spectra of GeV diamonds.

numerical integration of the spectra (just as was done when determining the critical wavelength for the split-spectrum intensity integration experiment).

With the diamond heated to various temperatures from T≈25 K to T≈45 K and spectra recorded at each temperature, calibration curves were constructed for these properties (fig. 3.8 (c)). These curves show precisions of 0.008 ± 0.0005 nm/K (central wavelength), 0.042 ± 0.003 nm/K (width), and 0.008 ± 0.0005 K^{-1} (amplitude). The values are in concordance with previous measurements.

With the diamond at room temperature, the ND was varied, allowing the beam to pump the diamonds at different powers. Fig. 3.9 (a) shows, predictably, that the diamond heating is linearly proportional to the pump power. Since increased power leads to increased sensitivity, but also incurs a heat penalty, another approach to increased sensitivity is must be considered. This approach is found in a sensitivity maximization function. This function is a linear summation of other weighted parameters, $S_{max} = \Delta\gamma + W_\lambda\Delta\lambda + W_A\Delta A$, where $\Delta\gamma$, $\Delta\lambda$, and ΔA are the precisions of width, central wavelength, and amplitude measurements, respectively. This S_{max} function minimizes the noise floor by choosing weights, W_λ and W_A, such that they minimize the variance of the measurements, $\sigma_S = \sqrt{{\sigma_\gamma}^2 + (W_\lambda\sigma_\lambda)^2 + (W_A\sigma_A)^2}$. As seen in fig. 3.9 (b), S_{max} produces a much lower noise floor than any of the individual properties on their own. Comparing changes

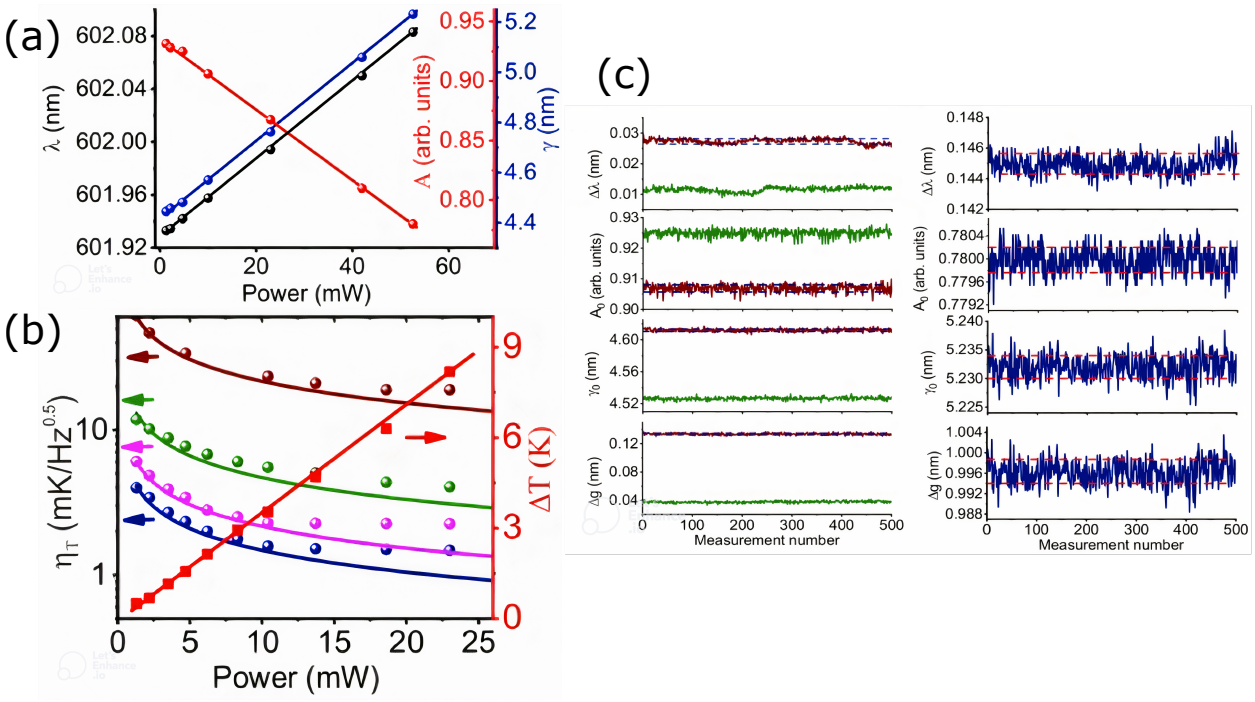

Figure 3.9: (a)Calibration curves for λ_0 (black), γ_0 (blue), and A_0 (red) as functions of power for Pl spectra of GeV diamonds. (b)Noise-floors for λ_0 (green), γ_0 (pink), A_0 (brown), and S_{max} (blue) as functions power compared with heating (red) as a function of power. (c)Traces for λ_0 ([i] and [v]), γ_0 ([iii] and [vii]), A_0 ([ii] and [vi]), and g ([iv] and [viii]) at pump powers of p ≈ 4.7 mW (brown lines in [i]-[iv]), p ≈ 10 mW (green lines in [i]-[iv]), and p ≈ 50 mW (blue lines in [v]-[viii]).

in noise floors with heating as functions of pump power, shows the inherent trade-off between heating and sensitivity in GeV temperature measurements. The traces in fig. 3.9 (c) confirm this sensitivity-to-power relationship. It is shown that, for p ≈ 23 mW, central wavelength, peak width and amplitude have sensitivities of 4, 2.3, and 19 mK/$\sqrt{\text{Hz}}$ respectively, with a few K of heating. At p ≈ 50 mW, a sensitivity of $\eta_T \approx 0.6$ mK/$\sqrt{\text{Hz}}$ was achieved, but the diamond suffered a heating penalty of $\Delta T \approx 10$ K.

The number of photons collected for a measurement is a product of the power of the pump and the length of time over which they are collected. Since the noise floor of the measurement is inversely proportional the square root of the number of photons collected, it can be lowered by either increasing pump power or acquisition time. This experiment has shown that, without sacrificing temporal resolution, in order to increase the sensitivity of GeV thermal measurements,

an increase in power is required. This power increase also delivers and increased heating penalty. For the best sensitivities, a heating penalty, that could be detrimental to *in vivo* measurements, is incurred.

3.4 Nickel–Vacancy open-air spectroscopy

Another split-vacancy color center being investigated is the nickel–vacancy (NiV) color center. It's structure is similar to the GeV, with the exception being an interstitial nickel atom replacing the germanium atom, as shown in fig. 3.10 (a). This color center has a central peak around 1.4 eV (880 nm) (fig. 3.10 (b)) which is in the near-IR.

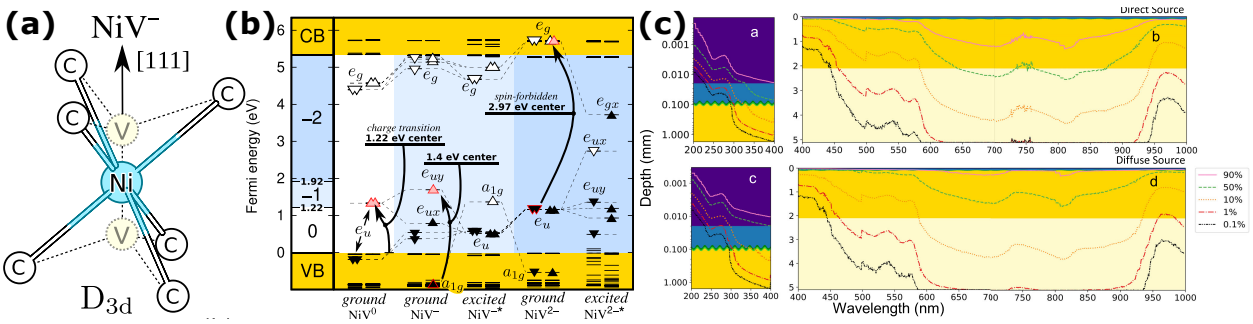

Figure 3.10: (a)A NiV is a color split vacancy color center with a nickel impurity.[22] (b) Kohn-Sham levels for NiV^- showing an excitation of 1.4 eV.[22] "Reprinted with permission from [22]." (c) In the near-IR, 10% fluence penetrates 4mm through biological material[23] "Reprinted with permission from [23]."

This near-IR peak is able to be pumped with a near-IR laser (780 nm). Since both the pump and peak are in the near-IR, they fall well within the biological transparency window. This allows them to penetrate biological material much better than the optical pump and signal photons from a GeV measurement, as is made clear in fig. 3.10 (c). This would allow thermal measurements to be taken at much greater depths in biological material than are possible with all-optical thermometry. Several specimens of microdiamonds, shown in fig. 3.11 (a), were found containing spectral peaks at 880 nm, indicating the presence of NiV's.

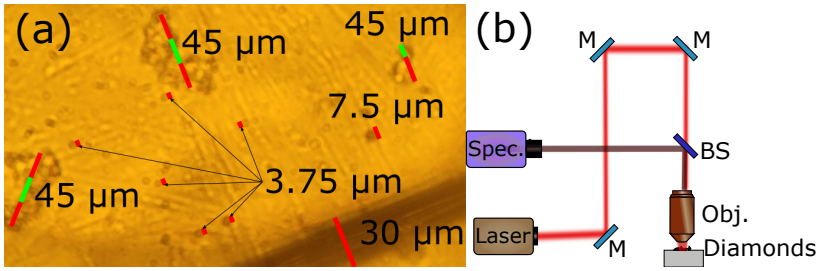

Figure 3.11: (a) Microdiamonds on the scale of around 5 microns, containing NiV color centers. (b) Several pump lasers (488 nm, 532 nm, 636 nm, and 780 nm) are focused onto a heated stage with NiV microdiamonds, whose fluorescence is reflected off of the beam splitter and collected by the spectrometer.

Fig. 3.11 (a) shows a wide-field microscope where an objective (obj.) focuses a pump laser onto a field of these diamonds on a heated stage. The objective then collects the diamond's fluorescence which reflects off the beam splitter (BS) and is collected by the spectrometer (SPEC). The use of a broadband beam splitter allows a wide range of lasers to be coupled into the system.

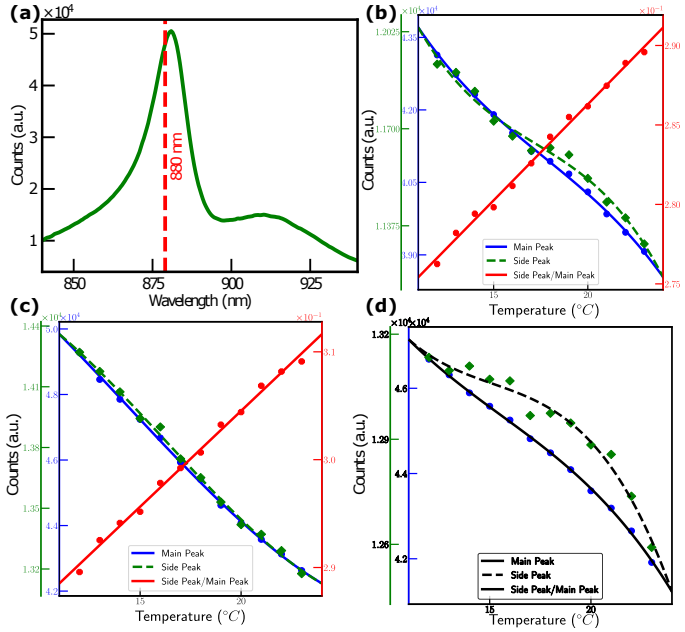

Figure 3.12: (a) Full spectrum of NiV with its main peak around 880 nm and a side peak around 910 nm. Tracking the temperature dependence of the amplitudes of the main peak, the side peak, and their ratios when pumped at (b)488 nm, (c) 532 nm, and (d) 636 nm

For initial measurements, amplitudes of the main peaks and the side peaks were measured, at various temperatures. Measurements were taken with three different optical lasers: 488 nm, 532 nm, and 636 nm. As shown in fig. 3.12 (b)-(d), regardless of pump wavelength, individual amplitude measurements were highly cubic in nature, while the temperature dependencies of the ratios are highly linear.

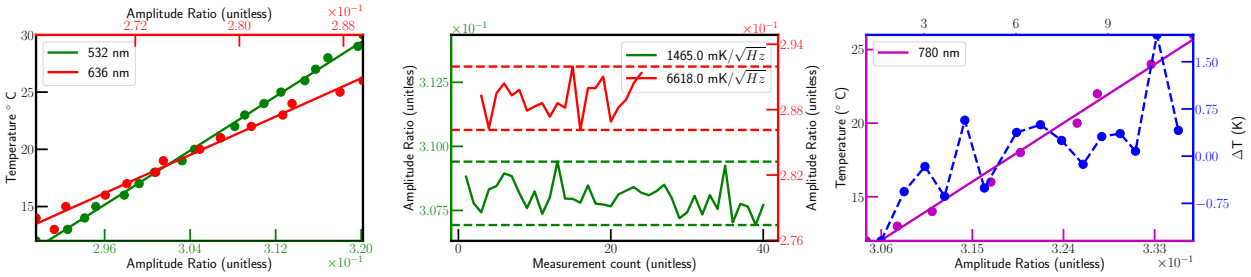

Figure 3.13: Calibration curves (a) and sensitivity measurements (b) for amplitude ratios pumped at 532 and 636 nm. (c) Calibration curve and laser power heating for amplitude ratios pumped at 780 nm

The calibration curves showed slopes of 592.35 K and 508.98 K, for 532 nm and 636 nm pumps, respectively (fig. 3.13 (a)). These curves were used to calculate sensitivities of 1465 $\mathrm{mK}/\sqrt{\mathrm{Hz}}$ and 6618 $\mathrm{mK}/\sqrt{\mathrm{Hz}}$ respectively (fig. 3.13 (b)). These unacceptably high sensitivities may be due to the fact that these are the first infrared spectroscopic measurements made in a lab that had, previously, only performed optical spectroscopy. It is highly possible that these sensitivities can be lowered with improved measurement practices. In fig. 3.13 (c), the calibration curve for the 780 nm pump shows a slope of 442.95 K, which was used to determine a relatively low heating penalty of less than 1 K over 5 mW of power.

With further refinement of equipment and measurement practices, improved data could be collected, leading to improved analyses of said data and better understanding of this largely unexplored color center.

4.1 applications

1. The GeV fiber probe modality could allow thermogenetics, in the same vein as the neurostimulation experiment mentioned earlier, to be performed without ODMR.

2. The split-spectrum intensity integration technique could be used to perform nanoscale bolometry, like the roundworm embryo experiment, without ODMR.

3. Fig. 4.1 shows a polymerase chain reaction (PCR) methodology in which a hollow fiber is filled with PCR materials and GeV nanodiamonds. A 532 nm laser is coupled into the fiber, which heats the diamonds and, in turn, the PCR solution. The fluorescence from the diamonds is collected, allowing the temperature to be measured. The power of the pump laser can be varied in accordance with the temperature measurements, providing the thermal cycle needed for the PCR multiply the desired species.[24]

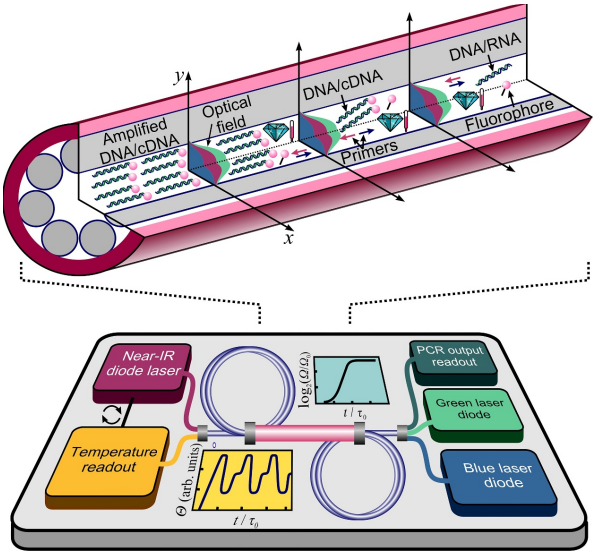

Figure 4.1: '*Photonic toolbox for fast real-time polymerase chain reaction*'[24] "Reprinted with permission from [24]."

4.2 Future explorations

4.2.1 Improved fittings

Improper spectral fittings can add noise to calculations which can propagate to noise in measurements calculated from said fittings. Currently, triple-Lorentzians are fit over the ZPL and PSB; however, the peak is more similar to a Lorentzian, from the homogeneous broadening of ZPL, mixed with a Gaussian, from the inhomogeneous broadening of the PSB. It is this observation which motivates the idea that better fits might be Voigt profiles, which are convolutions of a Lorentzian and a Gaussian distributions.

4.2.2 Optical gating

In the paper '*Optical Gating of Resonance Fluorescence from a single Germanium Vacancy Color Center in Diamond*', published by Chen et al in 'Physical Review Letters', a diamond with GeV's was placed in a cryostat with a confocal microscope. It was pumped with a non-resonant 532 nm laser as well as a 602.3 nm laser, which was resonant with one of the four GeV transitions.[25]

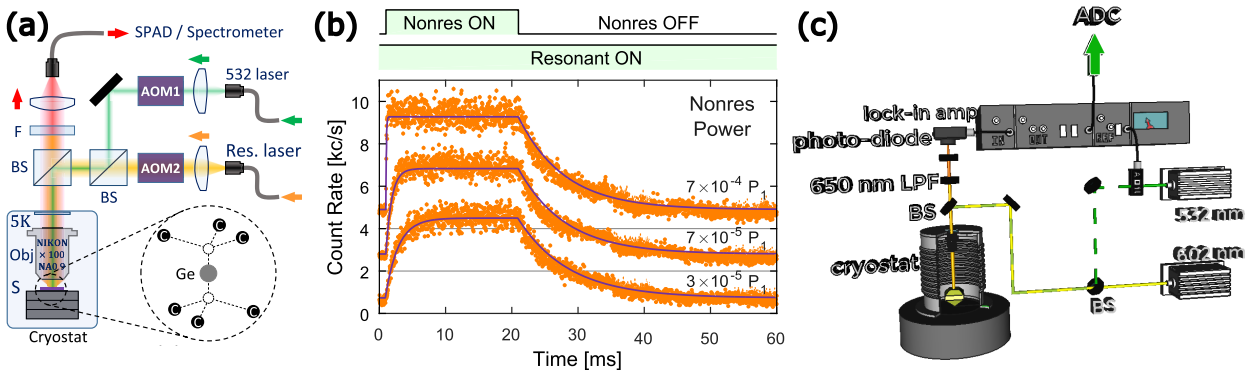

Figure 4.2: (a) A GeV diamond in a cryostat being pumped with resonant and non-resonant beams while its fluorescence is collected.[25] (b) While pumped with both beams, the color center fluorescence is brighter than when pumped by the resonant beam only.[25] "Reprinted with permission from [25]." (c) Using the LO in a LIA to control the AOM, allows the change of fluorescence to be recorded while filtering out the noise in the measurement.

The acousto-optic modulators (AOM) allow the switching of pumping modes from either one,

individually, to both, simultaneously. It was found that when pumping the GeV's with both lasers, the fluorescence was bright, while pumping the GeV's with just the resonant laser would cause the fluorescence to dim (fig.4.2(a)).

This behavior can be exploited by running the AOM on the resonant laser with the local oscillator (LO) on a lock-in amplifier (LIA), with the output of the photodiode being input into the LIA (fig.4.2(c)). In this measurement regime, the LIA would filter the noise and output a voltage that's the difference between the voltages output from the photodiode during bright and dim fluorescences. This value should be temperature dependent and could possibly provide another GeV thermometric measurement methodology, which a much lower noise floor.

4.3 Conclusion

Optical thermometry has been shown to have high spatial resolution, high sensitivity, high temporal resolution. Also, they're biologically inert, making them safe to put in living organisms. The most common optical thermometry is performed with ODMR performed on NV color centers. An improvement to that is the all-optical thermometry of split-vacancy color centers. These color centers have shown to have fluorescence spectral peaks with temperature dependent: peak amplitude, peak width, central wavelength, and DWF. They are able to achieve sensitivities on par with NV sensors, but suffer a heating penalty in exchange for it. Further investigation into the properties and behaviors of NiV's, could provide viable near-IR thermometry, allowing biologically deep fluorescence spectroscopy.

REFERENCES

[1] R. Mackenzie, "Early thermometry and differential thermometry," *Thermochimica Acta*, vol. 148, pp. 57–62, Aug. 1989.

[2] L. Hunt, "The early history of the thermocouple," *Platinum Metals Review*, vol. 8, no. 1, pp. 23–28, 1964.

[3] M. Hopcroft, B. Kim, S. Chandorkar, R. Melamud, M. Agarwal, C. Jha, G. Bahl, J. Salvia, H. Mehta, H. K. Lee, *et al.*, "Using the temperature dependence of resonator quality factor as a thermometer," *Applied physics letters*, vol. 91, no. 1, p. 013505, 2007.

[4] "Fisherbrand 10/30 ground joint thermometers - thermometers and temperature measurement, manual thermometers." `https://www.fishersci.com/shop/products/fisherbrand-10-30-ground-joint-thermometers-6/p-4555059#?keyword=`.

[5] M. Faraday, *Experimental researches in electricity: On Conducting Power Generally*, vol. 1. Royal Society of London, 1833.

[6] "Th10k 10 k thermistor." `https://www.thorlabs.com/thorproduct.cfm?partnumber=TH10K`.

[7] S. M. Blakley, A. B. Fedotov, J. Becker, N. Altangerel, I. V. Fedotov, P. Hemmer, M. O. Scully, and A. M. Zheltikov, "Stimulated fluorescence quenching in nitrogen–vacancy centers of diamond: temperature effects," *Optics Letters*, vol. 41, p. 2077, Apr. 2016.

[8] I. V. Fedotov, S. M. Blakley, E. E. Serebryannikov, P. Hemmer, M. O. Scully, and A. M. Zheltikov, "High-resolution magnetic field imaging with a nitrogen-vacancy diamond sensor integrated with a photonic-crystal fiber," *Optics Letters*, vol. 41, p. 472, Jan. 2016.

[9] S. M. Blakley, C. Vincent, I. V. Fedotov, X. Liu, K. Sower, D. Nodurft, J. Liu, X. Liu, V. N. Agafonov, V. A. Davydov, A. V. Akimov, and A. M. Zheltikov, "Photonic-crystal-fiber

quantum probes for high-resolution thermal imaging," *Phys. Rev. Appl.*, vol. 13, Apr. 2020.

[10] S. Blakley, X. Liu, I. Fedotov, I. Cojocaru, C. Vincent, M. Alkahtani, J. Becker, M. Kieschnick, T. Lühman, J. Meijer, P. Hemmer, A. Akimov, M. Scully, and A. Zheltikov, "Fiber-optic quantum thermometry with germanium-vacancy centers in diamond," *ACS Photonics*, vol. 6, pp. 1690–1693, July 2019.

[11] "What is hpht lab grown diamond?." `https://labrilliante.com/education/how-are-diamonds-grown/hpht`.

[12] M. Alkahtani, J. Lang, B. Naydenov, F. Jelezko, and P. Hemmer, "Growth of high-purity low-strain fluorescent nanodiamonds," *ACS Photonics*, vol. 6, pp. 1266–1271, Apr. 2019.

[13] P. R. Hemmer, "Engineering diamond color centers for quantum information and sensing (conference presentation)," in *Quantum Communications and Quantum Imaging XVII*, vol. 11134, p. 111340J, International Society for Optics and Photonics, 2019.

[14] Y. G. Ermakova, A. A. Lanin, I. V. Fedotov, M. Roshchin, I. V. Kelmanson, D. Kulik, Y. A. Bogdanova, A. G. Shokhina, D. S. Bilan, D. B. Staroverov, P. M. Balaban, A. B. Fedotov, D. A. Sidorov-Biryukov, E. S. Nikitin, A. M. Zheltikov, and V. V. Belousov, "Thermogenetic neurostimulation with single-cell resolution," *Nat. Commun.*, vol. 8, p. 15362, May 2017.

[15] J. Choi, H. Zhou, R. Landig, H.-Y. Wu, X. Yu, S. E. Von Stetina, G. Kucsko, S. E. Mango, D. J. Needleman, A. D. Samuel, *et al.*, "Probing and manipulating embryogenesis via nanoscale thermometry and temperature control," *Proceedings of the National Academy of Sciences*, vol. 117, no. 26, pp. 14636–14641, 2020.

[16] N. Wang, G.-Q. Liu, W.-H. Leong, H. Zeng, X. Feng, S.-H. Li, F. Dolde, H. Fedder, J. Wrachtrup, X.-D. Cui, S. Yang, Q. Li, and R.-B. Liu, "Magnetic criticality enhanced hybrid nanodiamond thermometer under ambient conditions," *Physical Review X*, vol. 8, Mar. 2018.

[17] G. Thiering and A. Gali, "Ab initio magneto-optical spectrum of group-IV vacancy color centers in diamond," *Phys. Rev. X.*, vol. 8, June 2018.

[18] Y. N. Palyanov, I. N. Kupriyanov, Y. M. Borzdov, and N. V. Surovtsev, "Germanium: a new catalyst for diamond synthesis and a new optically active impurity in diamond," *Sci. Rep.*, vol. 5, p. 14789, Oct. 2015.

[19] K. D. Jahnke, A. Sipahigil, J. M. Binder, M. W. Doherty, M. Metsch, L. J. Rogers, N. B. Manson, M. D. Lukin, and F. Jelezko, "Electron–phonon processes of the silicon-vacancy centre in diamond," *New Journal of Physics*, vol. 17, p. 043011, Apr. 2015.

[20] J.-W. Fan, I. Cojocaru, J. Becker, I. V. Fedotov, M. H. A. Alkahtani, A. Alajlan, S. Blakley, M. Rezaee, A. Lyamkina, Y. N. Palyanov, Y. M. Borzdov, Y.-P. Yang, A. Zheltikov, P. Hemmer, and A. V. Akimov, "Germanium-vacancy color center in diamond as a temperature sensor," *ACS Photonics*, vol. 5, pp. 765–770, Jan. 2018.

[21] H. X. Gao and L.-M. Peng, "Parameterization of the temperature dependence of the debye–waller factors," *Acta Crystallographica Section A Foundations of Crystallography*, vol. 55, pp. 926–932, Sept. 1999.

[22] G. Thiering and A. Gali, "Magneto-optical spectra of the split nickel-vacancy defect in diamond," *Physical Review Research*, vol. 3, Oct. 2021.

[23] L. Finlayson, I. R. M. Barnard, L. McMillan, S. H. Ibbotson, C. T. A. Brown, E. Eadie, and K. Wood, "Depth penetration of light into skin as a function of wavelength from 200 to 1000 nm," *Photochemistry and Photobiology*, vol. 98, pp. 974–981, Nov. 2021.

[24] C. Vincent, A. A. Voronin, K. Sower, V. V. Belousov, A. V. Sokolov, M. O. Scully, and A. M. Zheltikov, "Photonic toolbox for fast real-time polymerase chain reaction," *Laser Phys. Lett.*, vol. 17, p. 076202, July 2020.

[25] D. Chen, Z. Mu, Y. Zhou, J. E. Fröch, A. Rasmit, C. Diederichs, N. Zheludev, I. Aharonovich, and W.-B. Gao, "Optical gating of resonance fluorescence from a single germanium vacancy color center in diamond," *Phys. Rev. Lett.*, vol. 123, July 2019.

APPENDIX A

LIST OF PUBLICATIONS

1. Xinghua Liu, Ilya V Fedotov, Jiru Liu, Yusef Maleki, Chris Vincent, Sean M Blakley, and Aleksei Zheltikov, "Ultralow-power instant-on photon-pair counting and photon-entanglement analysis", Laser Phys. Lett. 18 045401 (2021)

2. Chris Vincent, A. A. Voronin, Kyle Sower, V. V. Belousov, Alexei Sokolov, Marlan Scully, and Aleksei Zheltikov, "Photonic toolbox for fast real-time polymerase chain reaction", Laser Phys. Lett. 17 076202 (2020)

3. Sean Blakley, Christapher Vincent, Ilya Fedotov, Xinghua Liu, Kyle Sower, Dawson Nodurft, Jiru Liu, Xiaohan Liu, Viatcheslav Agafonov, Valery Davydov, Alexey Akimov, and Aleksei Zheltikov, "Photonic-Crystal-Fiber Quantum Probes for High-Resolution Thermal Imaging", Phys. Rev. Applied 13, 044048 (2020)

4. Ilya Fedotov, M. A. Solotenkov, M. S. Pochechuev, A. A. Lanin, O. I. Ivashkina, K. V. Anokhin, Chris Vincent, Sean Blakley, M. A. Smirnov, S. A. Moiseev, S. Ya Kilin, Philip Hemmer, Alexey Akimov, Marlan Scully, A. B. Fedotov, and Aleksei Zheltikov, "All-Optical Quantum Biothermometry", ФОТОНИКА И КВАНТОВЫЕ ТЕХНОЛОГИИ (2020)

5. Sean Blakley, Xiaohan Liu, Ilya Fedotov, Ivan Cojocaru, Chris Vincent, Masfer Alkahtani, Joe Becker, Micheal Kieschnick, Tobias Lühman, Jan Meijer, Philip Hemmer, Alexey Akimov, Marlan Scully, and Aleksei Zheltikov, "Fiber-Optic Quantum Thermometry with Germanium-Vacancy Centers in Diamond", CS Photonics 2019, 6, 7, 1690–1693 (2019)

APPENDIX B

SUPPLEMENT 2: TEMPERATURE DEPENDENCE OF ELECTRON–PHONON PROCESSES IN SPLIT-VACANCY COLOR CENTERS AND THEIR EFFECTS ON SPECTRAL PEAK PROPERTIES

Jahnke et al built a microscopic model of the electron–phonon processes in silicon–vacancy (SiV) color centers for their paper, “Electron-phonon processes of the Silicon–Vacancy centre in diamond", published by Janhnke et al in the ‘New Journal of Physics’. This model explains the mechanisms behind the relationship between temperature and peak shift and broadening behaviors of the fluorescence emitted by SiV’s.[19] Although this treatment addresses SiV processes specifically, these properties are explanatory for similar behaviors in other Group IV color centers (including GeV’s).

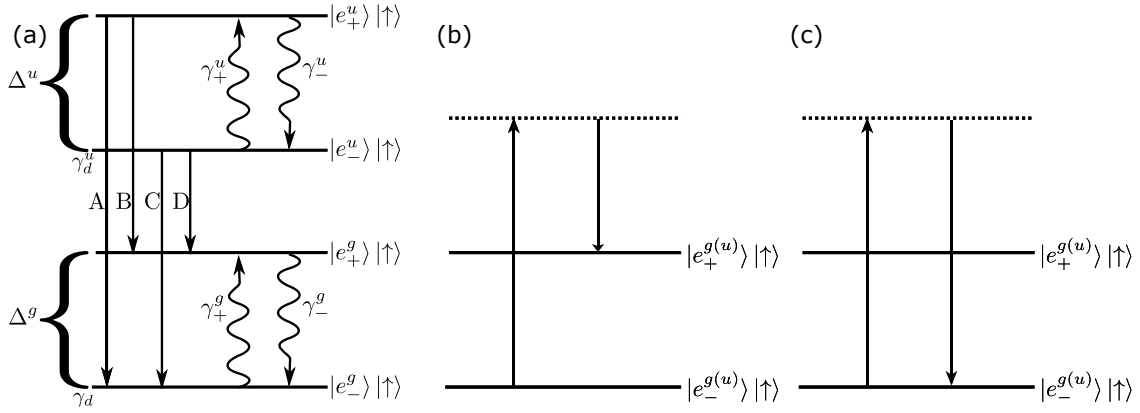

Figure B.1: (a)The standard spin up projection of the four energy levels,of a split-vacancy color center. This model includes 2 ground states($|e^g_{-(+)}\rangle$), with energy splitting of Δ^g and dephasing rate of γ^g_d, and 2 excited states ($|e^u_{-(+)}\rangle$), with energy splitting of Δ^u and dephasing rate of γ^u_d. This energy structure provides four radiative transitions (A,B,C,D) and four non-radiative transitions ($\gamma^u{}_+$, $\gamma^u{}_-$, $\gamma^g{}_+$, and $\gamma^g{}_-$). (b)Two-phonon inelastic Raman scattering. (c)Two-phonon elastic Raman scattering.

For Group IV split-vacancy color centers, assuming temperatures on the scale of $T \gg \frac{\hbar\Delta}{k_B}$, the

splitting of the ground and excited levels is determined by the linear Jahn-Teller interaction between E-symmetric electron states and acoustic phonons. Consider the following electron-phonon interaction:

$$\vec{\mathrm{V}}_{\mathrm{e}} = \sum_{\mathrm{k}} \hbar\chi_{\mathrm{k}} \left[\sigma_{+} \left(\mathrm{a}_{-,\mathrm{k}} + \mathrm{a}^{\dagger}{}_{-,\mathrm{k}}\right) + \sigma_{-} \left(\mathrm{a}_{+,\mathrm{k}} + \mathrm{a}^{\dagger}{}_{+,\mathrm{k}}\right)\right] \tag{B.1}$$

Here, χ_{k} is the interaction frequency for a single phonon, $\sigma_{+(-)}$ is the orbital state raising(lowering) operator. While $\mathrm{a}^{\dagger}{}_{\mathrm{p,k}}$ and $\mathrm{a}_{\mathrm{p,k}}$, for polarization $\mathrm{p} \in \{-, +\}$ and wave vector k, are the phonon creation and annihilation operators, respectively. In diamond color centers, the impurity ions are displaced and translated by long wavelength acoustic phonon modes with even parity. These modes are the ones responsible for electron–phonon coupling. When averaged over all modes such that $\omega_{\mathrm{k}} = \omega$, they have an interaction frequency of $\overline{|\chi_{\mathrm{k}}(\omega)|^2} \approx \chi\omega$, where χ is a proportionality constant. Also, the density of modes is $\rho(\omega) = \rho\omega^2$, with ρ being another proportionality constant.

B.0.1 Relaxation rates and peak broadening

Let $\partial\hat{\mathrm{V}}_{\mathrm{e}}/\partial \mathrm{t} = 0$, a single E phonon, with a frequency equal to level splitting ($\Delta^{\mathrm{g(u)}}$ in fig. B.1 (a)), will be absorbed or emitted as a first-order transition. After thermally averaging over initial states, summing over final states, and assuming temperatures such that $\mathrm{T} > \hbar\Delta/\mathrm{k_B}$, the relaxation rates are approximated to be linearly dependent on temperature, i.e.

$$\gamma_{+}^{\mathrm{g(u)}} \approx \gamma_{-}^{\mathrm{g(u)}} \approx \frac{2\pi}{\hbar}\chi\rho\Delta^2\mathrm{k_B T}$$

Fluorescent line broadening is determined by these relaxation rates and Jahnke et al found the broadening to be in line with these relaxation rates for $2.4\mathrm{K} < \mathrm{T} < 20\mathrm{K}$, but strayed from it beyond those temperatures. Indicating that, for temperatures greater than that range, relaxation rates are dominated by second-order electron–phonon transitions. Due to the form of equation B.1, the only

possible second-order electron–phonon transitions require identical initial and final states. This limitation suppresses, in split-vacancy color centers, the inelastic Raman scattering processes (fig. B.1 (b)) which dominate NV color centers, leaving the elastic Raman scattering processes (fig. B.1 (c)) as the only transition. Considering, then, the elastic scattering rate for $|\mathrm{e}_{-}\rangle$, and, again, thermally averaging over initial states and summing over final states, leads to

$$\gamma_{\mathrm{d}-} = 2\pi\hbar^2 \int_0^{\Omega} \mathrm{n}\left(\Delta+\omega,\mathrm{T}\right)\left(\mathrm{n}\left(\omega,\mathrm{T}\right)+1\right)\overline{\left|\chi_{\mathrm{K}}\left(\Delta+\omega\right)\right|^2}\,\overline{\left|\chi_{\mathrm{q}}\left(\omega\right)\right|^2}\left|\frac{1}{-\omega}+\frac{1}{\Delta+\omega}\right|^2 \rho\left(\Delta+\omega\right)\rho\left(\omega\right)\mathrm{d}\omega \tag{B.2}$$

With the Debye frequency of diamond being Ω. Under the conditions that acoustic modes and temperatures of the sort that exclusively modes with frequencies $\Omega \gg \omega \gg \Delta$ make up the vast majority of contributions to the integral in equation B.2, the relaxation rates can be rewritten as

$$\begin{aligned}\gamma_{\mathrm{d}-} \approx \gamma_{\mathrm{d}+} &\approx 2\pi(\hbar\Delta\chi\rho)^2 \int_0^{\infty} \mathrm{n}\left(\omega,\mathrm{T}\right)\left(\mathrm{n}\left(\omega,\mathrm{T}\right)+1\right)\omega^2\mathrm{d}\omega \\ &= \frac{2\pi^3}{3\hbar}(\Delta\chi\rho)^2\mathrm{k_B}^3\mathrm{T}^3\end{aligned}$$

This shows that the relaxation rates and, therefore, the peak broadening, goes like T^3.

B.0.2 Spin-orbit splitting and central wavelength shifts

Orbital state energies are also perturbed by electron–phonon interactions. $\delta\mathrm{E}_{-(+)}$, the second-order energy shifts for states $|\mathrm{e}_{-(+)}\rangle$, due to phonon modes, are

$$\delta \mathrm{E}_{-}\left(\mathrm{x}\left(\mathrm{y}\right),\mathrm{k}\right)=\left(\hbar\chi_{\mathrm{k}}\right)^{2}\left(\frac{\mathrm{n}_{\mathrm{x(y),k}}}{\omega-\Delta}-\frac{\mathrm{n}_{\mathrm{x(y),k}}+1}{\omega+\Delta}\right)$$

and

$$\delta \mathrm{E}_{+}\left(\mathrm{x}\left(\mathrm{y}\right),\mathrm{k}\right)=\left(\hbar\chi_{\mathrm{k}}\right)^{2}\left(\frac{\mathrm{n}_{\mathrm{x(y),k}}}{\omega+\Delta}-\frac{\mathrm{n}_{\mathrm{x(y),k}}+1}{\omega-\Delta}\right)$$

with wavevector k and occupation $\mathrm{n}_{\mathrm{x(y),k}}$. Using the assumptions from section B.0.1, concerning the acoustic modes and temperatures, and taking the thermal averages over all vibrations levels, it can be seen that

$$\begin{aligned}
\overline{\delta \mathrm{E}_{-}} &= \hbar^{2}\chi\rho\left(-\frac{1}{3}\Omega^{3}+\frac{\Delta}{2}\Omega^{2}+\frac{\left(\pi \mathrm{k_{B}}\right)^{2}}{3\hbar^{2}}\mathrm{T}^{2}\right)\\
\overline{\delta \mathrm{E}_{+}} &= -\hbar^{2}\chi\rho\left(\frac{1}{3}\Omega^{3}+\frac{\Delta}{2}\Omega^{2}+\frac{\left(\pi \mathrm{k_{B}}\right)^{2}}{3\hbar^{2}}\mathrm{T}^{2}\right)\\
\therefore \delta\Delta = \overline{\delta \mathrm{E}_{+}}-\overline{\delta \mathrm{E}_{-}} &= -\hbar^{2}\chi\rho\Delta\left(\Omega^{2}+\frac{2\left(\pi \mathrm{k^{B}}\right)^{2}}{3\hbar^{2}}\mathrm{T}^{2}\right)
\end{aligned}$$

This shows the splitting to be proportional to T^{2}; however, it has been experimentally shown to be proportional to T^{3}. The failure of this treatment to properly predict experimental data stems from an established problem in dealing with the linear Jahn-Teller interaction. Namely, the choice of rectangular coordinates in said treatment. The rectangular coordinates, $(\mathrm{Q_x}, \mathrm{Q_y})$, produce wavefunctions $\left(\psi_{\mathrm{i}}\left(\mathrm{Q_x}\right), \psi_{\mathrm{j}}\left(\mathrm{Q_y}\right)\right)$, where i and j are the independent mode numbers. Conflicts with the cylindrical symmetry of the linear Jahn–Teller vibrational potential, require higher orders of perturbation to achieve an accurate result.

This problem is alleviated with a switch to polar coordinates, ρ and ϕ, giving vibration wavefunctions $\psi_{\nu,\mathrm{l}}\left(\rho,\phi\right)$. These wavefunctions depend on principal vibrational quantum numbers, $\nu = 1, 2, 3, \ldots$, and vibrational angular momentum quantum numbers, $\mathrm{l} = -\nu+1, \ldots, 0, 1, \ldots, \nu-1$. In these coordinates, $\mathrm{E}_{\nu} = \nu\hbar\omega$ is the energy for modes of frequency ω and principal vibrational

quantum number ν. This gives that

$$\frac{1}{2}\left(\overline{\delta \mathrm{E}_{+}}+\overline{\delta \mathrm{E}_{-}}\right)=-2\hbar\chi\rho\int_{0}^{\Omega}\frac{2\mathrm{e}^{\hbar\omega/\mathrm{k_B T}}\left(\mathrm{e}^{2\hbar\omega/\mathrm{k_B T}}+3\right)}{\left(\mathrm{e}^{\hbar\omega/\mathrm{k_B T}}-1\right)\left(\mathrm{e}^{\hbar\omega/\mathrm{k_B T}}+1\right)^{2}}\omega^{2}\mathrm{d}\omega$$
$$\propto \mathrm{T}^{3}$$

Thusly, this approach does properly predict the experimental behavior, linking the second-order electron–phonon interactions in the color center with the shifting of the central wavelength of the fluorescence peak.